Luminal transport rates through intact endoplasmic reticulum limit the magnitude of localized Ca^{2+} signals

Cecile Crapart,[1] Zubenelgenubi C. Scott,[2] Tasuku Konno,[1] Aman Sharma,[2]
David M. D. Bailey,[1,3] Edward Avezov,[1,*] and Elena F. Koslover[2,*]

[1] *UK Dementia Research Institute at University of Cambridge, Department of Clinical Neurosciences, Cambridge CB2 0AH, United Kingdom*
[2] *Department of Physics, University of California, San Diego, La Jolla CA 92130*
[3] *Department of Zoology, Cambridge, United Kingdom*

The endoplasmic reticulum (ER) forms an interconnected network of tubules stretching throughout the cell. Understanding how ER functionality relies on its structural organization is crucial for elucidating cellular vulnerability to ER perturbations, which have been implicated in several neuronal pathologies. One of the key functions of the ER is enabling Ca^{2+} signalling by storing large quantities of this ion and releasing it into the cytoplasm in a spatiotemporally controlled manner. Through a combination of physical modeling and live-cell imaging, we demonstrate that alterations in ER shape significantly impact its ability to support efficient local Ca^{2+} releases, due to hindered transport of luminal content within the ER. Our model reveals that rapid Ca^{2+} release necessitates mobile luminal buffer proteins with moderate binding strength, moving through a well-connected network of ER tubules. These findings provide insight into the functional advantages of normal ER architecture, emphasizing its importance as a kinetically efficient intracellular Ca^{2+} delivery system.

I. SIGNIFICANCE STATEMENT

Cells make use of Ca^{2+} ions to transfer information and regulate many cell functions. By modulating Ca^{2+} levels, timing, and location in the cytosol, cells can encode a wide diversity of signals with this single ion. The ER constitutes a major intracellular Ca^{2+} store, extending throughout the entire cell as a network of tubules through which Ca^{2+} ions and Ca^{2+}-binding buffer proteins can move. This work demonstrates that mobile buffer proteins and a well-connected lattice-like architecture of the ER network are optimal to supply local Ca^{2+} signals and that changes in ER structure can modulate Ca^{2+} release. Consequently, a key structure-function link is suggested for the ER network, relying on its performance as an intracellular transport system for bioactive material.

II. INTRODUCTION

The endoplasmic reticulum (ER) is a membrane-enclosed organelle with characteristic structural subdomains, including stacks of membranous sheets contiguously interconnected with a network of tubules, all sharing a common lumen. ER sheet morphologies convey a clear functional advantage by maximizing surface area to accommodate ribosomes for secretory protein synthesis [1, 2]. However, the functional role of the highly looped interconnected architecture of the peripheral ER network remains obscure. This knowledge gap hinders our understanding of the diseases associated with ER shaping proteins. In particular, mutations in ER morphogens cause Hereditary Spastic Paraplegia and ALS (motor neuron diseases) [3] and their protein level alterations are associated with Alzheimers disease [4, 5]. The apparent selective vulnerability of neuronal cells, with their extensive ER tubule-containing periphery, has not been mechanistically rationalized.

It is expected that the normally shaped and functioning cell-wide network of ER tubules allows delivery of bioactive molecules, including proteins, lipids and Ca^{2+} ions, for signalling or supply to other organelles [6–8]. This concept highlights the need to elucidate if and how the morphology of the ER modulates its function as an intracellular transport network, particularly its role in the delivery of Ca^{2+} for signalling events. ER-facilitated Ca^{2+} signaling enables selective regulation of diverse processes in numerous cell types: local Ca^{2+} transients ("puffs", originally detected in Xenopus oocytes during maturation [9, 10]) are detectable in cultured cell lines (eg: HeLa [11], SHSY5Y [12]), pancreatic acinar cells accompanying secretion, [13] and smooth muscle cells, governing contraction/relaxation [14, 15]. Localized Ca^{2+} transients and microdomains also play critical roles in healthy neuronal and astrocytic signaling [16–20].

The role of the ER in Ca^{2+} signaling is facilitated by its Ca^{2+} storage capacity: the narrow ER lumen holds free and protein buffer-bound Ca^{2+} at concentrations three orders of magnitude higher than the cytoplasm. The ions can be released from the ER on demand through the opening of inositol 1,4,5-triphosphate receptor-channels (IP3Rs) [11, 21] or ryanodine receptors (RyRs) [22]. Channel opening can generate Ca^{2+} responses of various extent, ranging from elementary local Ca^{2+} signals upon opening of a single or a few IP3Rs [23, 24], to large-scale events that can propagate throughout the cell as a saltatory wave via Ca^{2+}-induced Ca^{2+} release [25, 26]. Modeling studies have highlighted the importance of Ca^{2+}

* Authors for correspondence: ea347@cam.ac.uk (EA), ekoslover@ucsd.edu (EFK)

channel distribution and opening probabilities in governing the magnitude of the elementary signaling events [27–30].

Crucially, ER Ca^{2+} signalling requires enough free ions available to steeply raise the local cytosolic Ca^{2+} levels [31]. The release of Ca^{2+} ions must work against several offsetting effects: strong dilution due to their rapid diffusion in the cytoplasm [32], cytoplasmic buffering [33], and active clearing/reuptake [34]. This raises the question of whether the ER can sustain an adequate supply of Ca^{2+} for release by drawing exclusively on its local pool, or whether local release events require tunnelling of the ion from more distant ER regions. In the latter case, we expect the Ca^{2+} signalling activity to be dependent on characteristics that determine the efficiency of transport and mixing of luminal content, including network connectivity and the kinetic parameters of motion through the ER lumen. Since the vast majority of ER luminal Ca^{2+} is bound to abundant high-capacity buffer proteins (e.g. calreticulin, with 25 Ca^{2+} binding sites [35]), the mobility and binding affinity of the carrier proteins may also serve as potentially important parameters for optimizing Ca^{2+} release efficiency.

To gain a quantitative understanding of the impact of intra-ER luminal transport on localized Ca^{2+} release, we constructed a coarse-grained physical model that incorporates localized permeability of the ER membrane to Ca^{2+} ions, equilibrated binding of luminal Ca^{2+} to buffer sites, and diffusive and active transport through a tubular network geometry. The model reveals that rapid Ca^{2+} release requires mobile buffer proteins with a relatively low binding strength, transported through a well-connected ER network lattice. Further, to validate the predictions of the *in silico* model, we have established a set of tools to perturb various aspects of ER structure via morphogen manipulation, leading to partial luminal fragmentation through tubule narrowing or increase in tubule length through junction depletion. Using all-optical imaging of Ca^{2+} dynamics and fluorescence lifetime imaging (FLIM) measurements of Ca^{2+} concentrations in absolute terms allows exploration of how Ca^{2+} handling in the ER depends on its modified morphology. The resulting experimental data confirm that morphological changes elicited by ER-shaping gene manipulations result in slower luminal material transport and consequently smaller local Ca^{2+} releases. These results provide a functional role for the complex architecture of the ER network as an intracellular Ca^{2+} transport system. The conceptual framework presented here can help establish the optimal ER structure for various physiological conditions and rationalize pathologies associated with ER perturbations.

III. RESULTS

A. Purely local Ca^{2+} release is insufficient to raise cytoplasmic levels

To explore how the Ca^{2+} release function of the ER is dependent on its structural features, we set out to model the various physical effects that govern local Ca^{2+} currents out of the lumen. We begin with a maximally simple aspatial model that incorporates equilibrated luminal buffer binding, an effective coarse-grained permeability for Ca^{2+} through the ER membrane, and dilution upon cytoplasmic release. In this initial model, the intra-ER transport is not included. Our goal is to establish the extent to which spatiotemporal elevation of cytoplasmic Ca^{2+} can be achieved by the locally available pool in the ER lumen.

In the purely local model, an isolated region of ER (radius $R = 0.25\mu$m) maintains a well-mixed lumen and releases Ca^{2+} into the cytoplasm with permeability P (Fig. 1a). The effective permeability parameter (units of μm/s) subsumes details of individual channel densities and opening probabilities [36]. The cytoplasm is treated as a bulk three-dimensional continuum. The release region contains a length L of ER tubules with radius r. The scaling of tubule length with the size of the release region depends on the architecture of the network. Here we consider a small region surrounding a junction node, which yields an estimate of $L \approx 3R$. Given the narrow width of ER tubules, the ratio of ER lumen to cytoplasmic volume in this region is very small: $V_{\mathrm{ER}}/V_{\mathrm{cyto}} \approx 3r^2L/4R^3 \approx 0.09$. Furthermore, over time the released Ca^{2+} will spread out through the three-dimensional cytoplasm, implying that local cytoplasmic Ca^{2+} elevation must be quite limited despite the high concentration of ER luminal Ca^{2+}. Such dilution effects are known to underlie the relatively low elevation of cytoplasmic Ca^{2+} as compared to luminal Ca^{2+} levels [37]. The presence of active clearance mechanisms such as extrusion through plasma membrane pumps or ER re-uptake would limit the cytoplasmic Ca^{2+} still further [38]; these effects are not included in our model, which thus sets a conservative bound on cytosolic Ca^{2+} levels.

The Ca^{2+} capacity of the ER lumen is greatly enhanced by the presence of Ca^{2+}-binding buffer proteins, such as calreticulin, PDI, GRP94, and others [39]. Many of these buffer proteins contain domains with high capacity and low affinity for Ca^{2+} storage. For example, each calreticulin protein contains approximately 25 Ca^{2+} binding sites [35, 40]. We take the buffer protein concentration in the lumen to be approximately 0.1mM, based on prior measurements of calreticulin densities [41]. The steady-state free $[Ca^{2+}]_{\mathrm{ER}}$ is set to $U_0 \approx 0.5$mM, a typical value within the range of published values [42–44], and in agreement with our own measurements (see below). Thus, the concentration of buffer binding sites is $5\times$ greater than the free Ca^{2+} concentration. Because

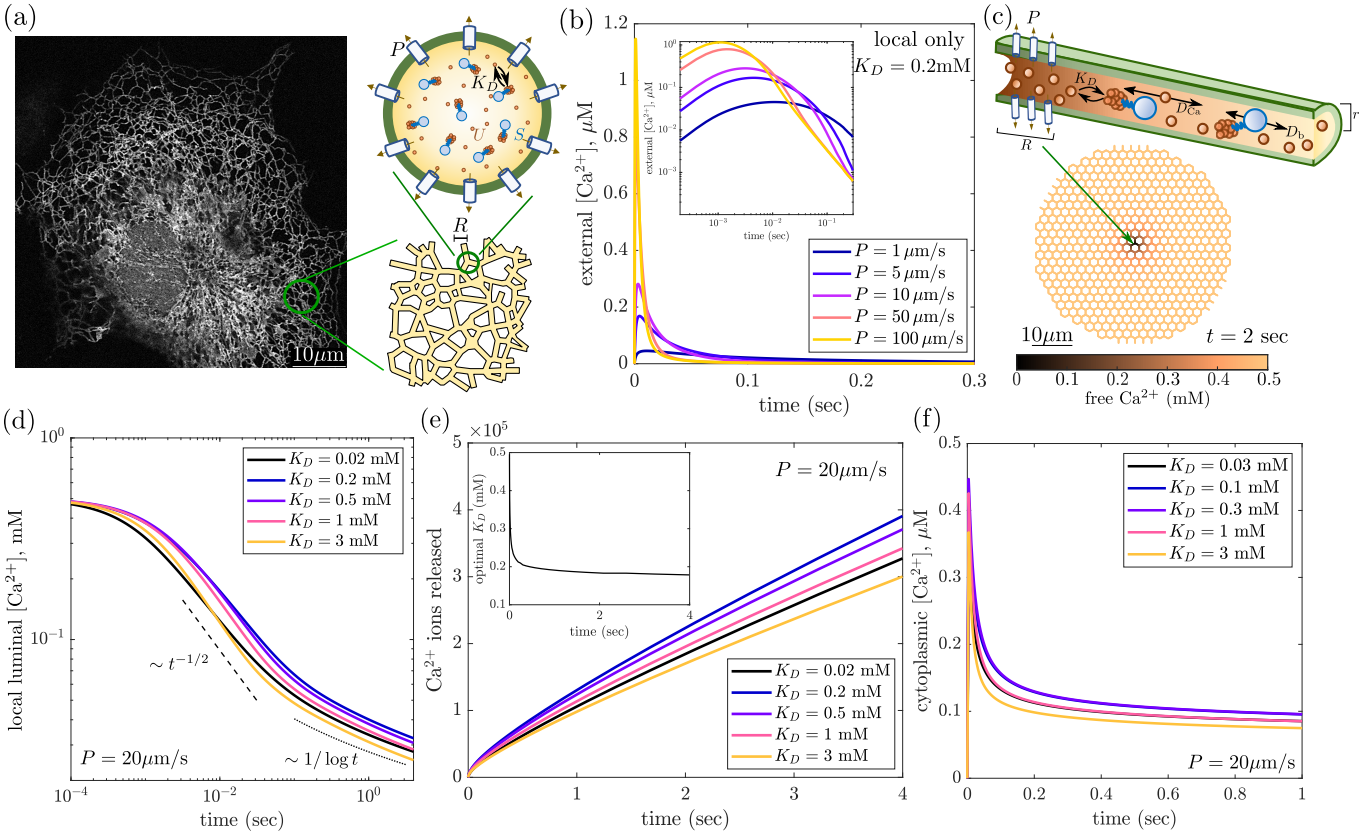

FIG. 1. Ca^{2+} release requires transport through tubular network and depends on buffer strength. (a) Sample image of peripheral ER network in COS-7 cell. Initial model represents local Ca^{2+} releasing region as a well-mixed domain. (b) Cytoplasmic Ca^{2+} levels predicted from well-mixed model, showing very low local Ca^{2+} events magnitudes from release of only locally available Ca^{2+}, for different values of permeability P. Inset shows same curves on log-log axes. (c) Snapshot of spatially resolved model for Ca^{2+} release from a honeycomb network structure. Color corresponds to free luminal Ca^{2+}. (d) Average free $[Ca^{2+}]_{ER}$ in local release region plotted over time for different values of buffer binding strength K_D. Dashed line shows short-time scaling expected for 1D delivery through tubules. Dotted line shows long-time scaling expected for 2D delivery. (e) Cumulative amount of Ca^{2+} ions released from the network over time, for different values of K_D (legend as in d). Inset shows optimal K_D value for maximum cumulative Ca^{2+} released as a function of time. (f) Average cytoplasmic Ca^{2+} concentrations after release, averaged over a sphere of $R_{loc} \approx 1\mu m$. Default parameter values are $P = 20\mu m/s$, $S = 2.5mM$, $R = 0.25\mu m$. Cytoplasmic spread assumes $D_{cyto} = 200\mu m^2/s$, $R_{loc} = 1\mu m$.

only soluble ions can be released through channels in the ER membrane, the overall dynamics of ER Ca^{2+} release depends on the interplay between buffer-bound and unbound Ca^{2+}.

Assuming that Ca^{2+} binding is equilibrated at all times, the evolution of free Ca^{2+} concentration (derived in Methods) can then be expressed as:

$$\frac{dU}{dt} = \frac{-(2P/r)U}{1 + \frac{SK_D}{(U+K_D)^2}}, \tag{1}$$

where U is the free $[Ca^{2+}]_{ER}$, S is the total concentration of buffer sites, K_D is the equilibrium dissociation constant, P is the effective membrane permeability, and r is the ER tubule radius. This expression is integrated to give the free Ca^{2+} levels in the lumen over time, and hence the Ca^{2+} release current $J(t) = 2\pi rLPU(t)$ from the well-mixed local ER region.

To model the local Ca^{2+} concentrations in the cytoplasm, we assume that Ca^{2+} ions diffuse outward from a point-like release source, and that the measured cytoplasmic concentration is averaged over a sphere of radius R_{loc} surrounding the source (details in Methods). The cytoplasmic Ca^{2+} concentration profile (Fig. 1b) displays a peak at very short times (few ms), followed by a steep decline. This decline arises from a combination of Ca^{2+} depletion in the lumen and the dilution effect of the released Ca^{2+} spreading out over ever-larger volumes. We do not include the effect of active pumps that remove Ca^{2+} from the cytoplasm, which would lower the cytoplasmic levels still further. Notably, plugging in physiologically relevant parameters implies that the maximum released Ca^{2+} concentration is generally sub-μM, orders of magnitude lower than the Ca^{2+} concentration within the ER.

Cytoplasmic Ca^{2+} concentrations drop sharply over

subsecond time-scales. After a time of 0.1 seconds post-release, the local Ca^{2+} concentration is expected to be below 20nM regardless of the permeability for releasing Ca^{2+} from the ER. We note that binding to cytoplasmic buffer proteins is known to slow the spreading of Ca^{2+} in the cytoplasm [45, 46]. However, such binding must also reduce the free Ca^{2+} levels surrounding the release site [37]. In Supplemental Material Fig. S1, we show that cytoplasmic buffering does not substantially raise the local free Ca^{2+} concentration. The minimalist model presented here thus sets a limit on cytoplasmic Ca^{2+} concentrations following a purely local release event.

The magnitudes of localized Ca^{2+} release events from the ER have been estimated to range from ~ 30nM (for single-channel 'blips'), to ~ 200nM (for 'puffs' in oocytes and 'sparks' in cardiomyocytes) [42, 47–49], to puffs of up to 1μM in osteoclasts [27]. Furthermore, the spatial extent of the Ca^{2+} releasing region in puff events has been estimated as diffraction-limited ($R \approx 0.25\mu$m) [28, 29]. Using our estimated parameters, the total amount of luminal Ca^{2+} in a region of this size around an ER junction is only about 10^4 ions. By contrast, the amount of Ca^{2+} released in oocyte blips and puffs has been estimated at $10^5 - 10^6$ ions [29]. Achieving these transient elevations of cytoplasmic Ca^{2+} would require a complete loss of the local luminal pool, necessitating transport through the ER.

While we use a modest estimate for the luminal Ca^{2+} carrying capacity, increasing the density of binding sites by an order of magnitude (to ~ 1mM buffer protein concentration) is still not sufficient to raise cytoplasmic levels above 200nM (Supplemental Fig. S2). Thus the locally available pool of Ca^{2+} is insufficient to sustain local release events, and the ions must tunnel through the lumen from neighboring regions of the ER network.

B. Network transport and moderate buffer strength combine to enable sustained release

Since local Ca^{2+} is insufficient to produce measured puff magnitudes, we next consider the effect of transport through the lumen of the ER network. We extend our initial well-mixed system into a spatially-resolved reaction-diffusion model for Ca^{2+} ions and buffer proteins within a network of tubules with a locally permeable release region. The peripheral ER in adherent mammalian cells forms a highly looped lattice-like planar network structure (Fig. 1a). We represent this morphology with a honeycomb network (Fig. 1c) with edge length $\ell = 1\mu$m [30, 50] and tubule radius $r = 50$nm [8, 51]. A local release region, with permeability P for free Ca^{2+} ions, is taken to have a radius of $R = 0.25\mu$m, as suggested for measurements of Ca^{2+} puffs in *Xenopus* oocytes [28].

Both free Ca^{2+} ions and buffer proteins are assumed to diffuse through the ER tubules. We use prior estimates of diffusivity for ER luminal proteins as $D_b \approx 3\mu\text{m}^2/\text{s}$ [8], and free Ca^{2+} ions are assumed to diffuse an order of magnitude faster [46], at $D_{\text{Ca}} \approx 30\mu\text{m}^2/\text{s}$. The reaction-diffusion equations relating concentrations of free ions $U(x,t)$, total ions $C(x,t)$, and total buffer sites $S(x,t)$ are:

$$\begin{aligned} \frac{dC}{dt} &= D_{\text{Ca}}\frac{\partial^2 U}{\partial x^2} + D_b\frac{\partial^2}{\partial x^2}(C-U) - v\frac{\partial C}{\partial x} - \frac{2P}{r}UH(x) \\ \frac{dS}{dt} &= D_b\frac{\partial^2 S}{\partial x^2} - v\frac{\partial S}{\partial x}, \end{aligned} \tag{2}$$

where H is an indicator function equal to 1 in the permeable region and 0 otherwise, and the advective term is removed (flow velocity $v = 0$) for purely diffusive transport. For the purely diffusive case, the concentration of total buffer sites S is spatially constant at all times. Assuming instantaneous equilibration between bound and unbound ions gives a direct relation between U, C, and S (see Methods), completing the system of equations. These equations are solved numerically along the effectively one-dimensional tubules of the network, using a finite volume method (details in Methods).

The release of Ca^{2+} from the network proceeds in several phases (Fig. 1d). At very short times the local luminal free Ca^{2+} levels are maintained by release from the buffer sites. Next, there is a subsecond time period during which Ca^{2+} is transported through one-dimensional (1D) tubules to the permeable zone. Standard solutions of the 1D diffusion equation imply that the concentration near an absorbing region scales as $\sim t^{-1/2}$ [52]. On longer time periods of roughly $0.1 - 10$sec, delivery of Ca^{2+} to the release site involves transport over the two-dimensional (2D) network. This leads to local concentrations that drop as $1/\log t$, so that the luminal free Ca^{2+} is very slowly depleted over this range of time scales.

The Ca^{2+} delivery dynamics can also be seen by plotting the total amount of Ca^{2+} released (Fig. 1e), where a rapid release over millisecond timescales is followed by a release rate that changes very slowly over the course of multiple seconds. The cytoplasmic Ca^{2+} surrounding the release site (Fig. 1f) also demonstrates a peak at tens of milliseconds, followed by a slow decay as 2D transport of Ca^{2+} through the network does not keep up with 3D dilution in the cytoplasm. Notably, the levels of cytoplasmic Ca^{2+} at second timescales in this model are an order of magnitude higher than those predicted for purely local Ca^{2+} release (Fig. 1b vs f), highlighting the importance of transport through the network.

A key assumption of our model is that the initial concentration of free Ca^{2+} in the ER lumen (U_0) is kept constant regardless of the buffer strength, which in turn modulates the total Ca^{2+} storage capacity. This assumption relies on the notion that the various mechanisms responsible for maintaining luminal Ca^{2+} homeostasis will respond to free Ca^{2+} rather than total Ca^{2+} concentrations. An important consequence is that as the buffer site binding becomes stronger (lower K_D), the total initial Ca^{2+} in the system increases, up to the maximum

carrying capacity defined by the concentration of buffer binding sites. The amount of Ca^{2+} released over time has a non-trivial dependence on the buffer strength. When the buffer strength is well-matched to the free Ca^{2+} concentration ($K_D \approx U_0$), the initial levels of free Ca^{2+} can be robustly maintained in the lumen as the release proceeds. However, stronger binding (lower K_D) enables a greater total Ca^{2+} storage capacity in the ER so that there is more Ca^{2+} to be released.

Overall, an optimum intermediate value K_D^{opt} maximizes both the amount of released Ca^{2+} and its cytoplasmic elevation. This optimal value is robust over a broad range of probe times during which the release is measured (Fig. 1e, inset). In the initial phase of rapid release, $K_D^{\text{opt}} = 0.5$mM provides optimal buffering for the localized release region. In the infinite-time limit, when the lumen becomes fully depleted of Ca^{2+}, an arbitrarily small value of K_D becomes optimal since it allows storage of the maximum amount of total Ca^{2+} in the lumen. However, in the transport-dominated phase, the local concentration of free Ca^{2+} decreases slowly as the effectively two-dimensional transport through the network replenishes the leakage in the permeable region. Over a range of $0.1 - 10$sec, an intermediate value of $K_D \approx 0.2$mM is optimal both for maximum Ca^{2+} release and maximal cytoplasmic Ca^{2+} elevations (Fig. 1e,f). The effect of the optimal K_D is enhanced if there is a higher density of luminal buffer binding sites than the modest estimate used here (Supplemental Material Fig. S3). The value of the optimal binding strength is largely independent of the assumed buffer site density. Its dependence on the permeability and size of the local release region is described in Supplemental Material Fig. S4.

Notably, the luminal Ca^{2+}-binding protein calreticulin contains high-capacity Ca^{2+} binding sites with a moderate binding affinity ($K_d \approx 0.25$mM [53]). This value matches well to the optimal binding strength found in our model system. The model thus provides a potential explanation for the limited binding strength of these Ca^{2+} buffers, by demonstrating the increased efficiency of local Ca^{2+} release associated with relatively weak binding.

C. Buffer protein mobility enhances Ca^{2+} release

The transport of Ca^{2+} ions through the extended ER lumen to the local release site involves a combination of rapid free ion diffusion, and the slower diffusion of the Ca^{2+}-binding buffer proteins which carry the majority of luminal Ca^{2+}. Although much slower than the Ca^{2+} ions, the mobility of buffer proteins does contribute to the flux of Ca^{2+} release, on timescales beyond the initial emptying of the local region (Fig. 2a). The effect of buffer diffusivity is particularly important when buffer strength is tuned to its optimal value (Fig. 2b).

Recent measurements of single-particle trajectories for luminal proteins have indicated that such proteins can traverse individual ER tubules much more rapidly than would be expected from diffusion alone [54]. The observed dynamics of luminal particles is consistent with the action of persistent randomly-directed runs across individual ER tubules, possibly associated with short-range luminal flows, giving rise to a model of the ER as an active network [55]. This interpretation was further supported by the apparently superdiffusive spatiotemporal spreading of photoactivated luminal proteins [8]. We therefore consider the effect on Ca^{2+} transport and release of randomly directed flows of velocity v, which flip direction independently for each individual edge, as a Poisson process with timescale τ. Particles move through this network with a combination of diffusive motion and advection by the edge flows. The rapid flow velocity along the edges is set to $v = 20\mu$m/s, as previously reported for short-range processive movements of luminal proteins in ER tubules [54].

For sufficiently long times ($t \gg \tau$), individual particles on such an active network undergo random walks that give rise to an effectively diffusive motion. We leverage agent-based simulations to demonstrate a linear scaling of the mean-squared displacement (MSD) for particles moving along an active network, consistent with long-range diffusive behavior (Fig. 2c). The effective diffusivity can be estimated from the slope of the MSD over time. Notably, the effective diffusivity of particles is highest at an intermediate value of the flow switching time τ (Fig. 2d). Flows that switch too quickly result in particles retracing their path many times along a single edge, resulting in little net effect on the diffusivity. Alternately, flows that persist too long tend to trap particles at nodes with converging flows, also decreasing their rate of spread over long distances. The existence of an optimal switching timescale was previously noted in the context of mean first passage times on active networks [55]. The optimum switching time for particle spreading is one that allows the flow directionality to persist long enough for the particle to encounter a 'trap' with converging flow, but not much longer. For a network with primarily degree-3 nodes, such as described here, a particle will cross on average 4 edges prior to encountering a trap. For the rapid velocities considered, this would correspond to an optimal switching time of $\tau^{\text{opt}} \approx 0.2$sec, corresponding to the time-scale of transition between traps. Our simulations show a peak in the effective diffusivity at switching times comparable to τ^{opt} (Fig. 2e).

A dimensionless quantity that describes the importance of flow versus diffusion is the Péclet number: $\text{Pe} = vL/D$, where v is the flow velocity, D the diffusivity, and L a length scale of interest. A value of $\text{Pe} \gg 1$ indicates that transport is primarily driven by flow, while $\text{Pe} \ll 1$ implies that diffusion is dominant and the flow makes no noticeable difference over that length scale. For the case of free Ca^{2+} ions moving over a single network edge, we estimate $\text{Pe} \approx 0.7$, implying that the putative luminal flows will have little effect on the free ion transport. However, for buffer proteins, the corresponding Péclet number is an order of magnitude higher ($\text{Pe} \approx 7$).

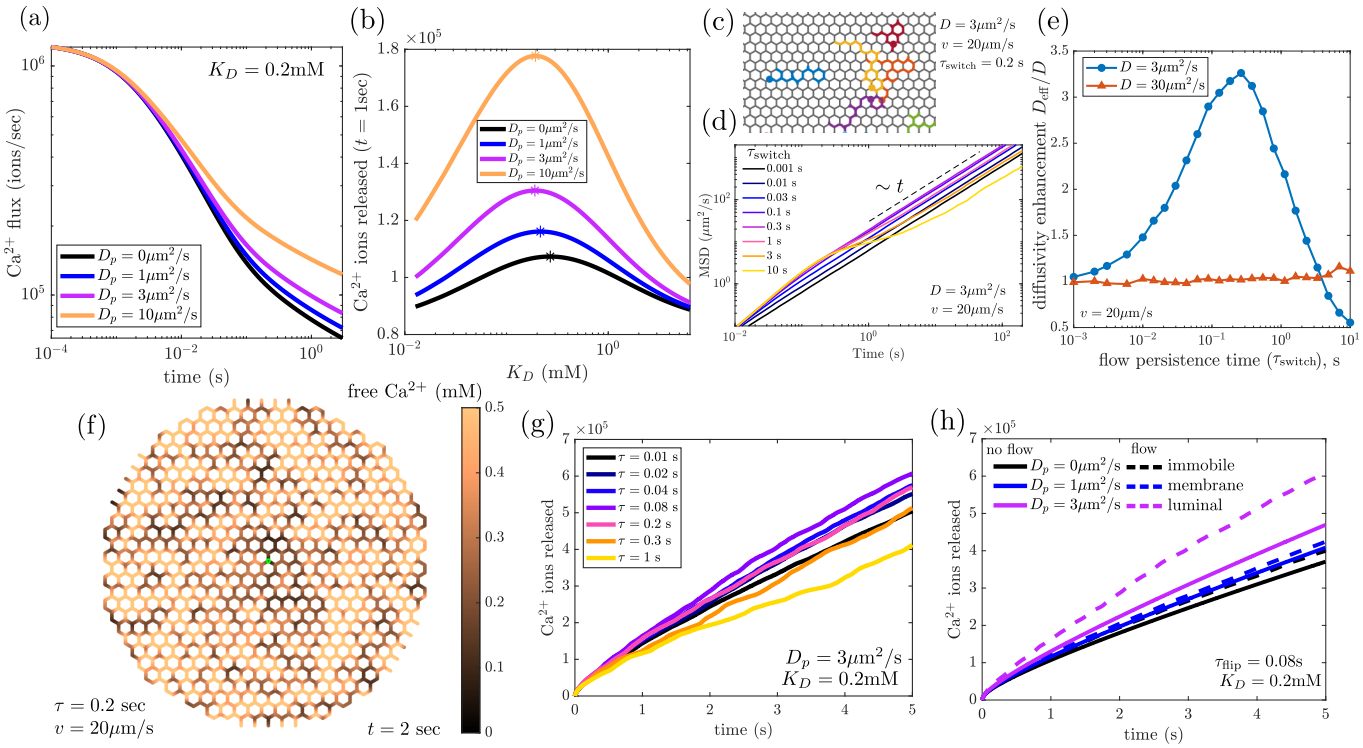

FIG. 2. Mobility of buffer proteins and active luminal flow can enhance local Ca^{2+} release. (a) Ca^{2+} flux out of local release region in a honeycomb network, for different values of buffer protein diffusivity. (b) Cumulative Ca^{2+} ions released in a 1sec interval, as a function of buffer binding strength K_D, for different protein diffusivities. (c) Example trajectories of individual simulated proteins on a honeycomb network with active flows. (d) Mean-squared displacement of simulated particles on active network. (e) Scaled effective long-time diffusivity D_{eff}, as a function of the active flow persistence time. (f) Snapshot of free Ca^{2+} concentrations in an active network, with local release region marked as green dot. (g) Cumulative Ca^{2+} released over time in an active network with flow velocity $v = 20\mu$m/s, and different persistence times τ_{switch}, demonstrating maximum release with flows of intermediate persistence. Each curve is averaged over 10 independent realizations of dynamic random flow patterns. (h) Cumulative Ca^{2+} released over time for different values of buffer diffusivity, with active flows (dashed lines) or without them (solid lines). Black and blue curves correspond to immobile and membrane bound buffer proteins, which are not subject to luminal flow.

Consequently, we would expect active flow of the luminal contents to substantially enhance the spreading of Ca^{2+}-binding buffer proteins but not the free ions themselves.

In Fig. 2g we plot the cumulative release of Ca^{2+} in a network with random active flows along its tubules (Fig. 2f). We see that flows with a persistence time of $\tau \approx 0.08$s allow for the most rapid local Ca^{2+} release. This value is roughly half the peristence time that optimizes long-range diffusivity (Fig. 2e), presumably due to the advantage of rapid flipping in short-range delivery of Ca^{2+} from the edges directly connected to the release site.

By contrast, when buffer proteins are immobilized, the Ca^{2+} release is substantially slower and largely unaffected by flow (Fig. 2h). Similar results are seen if we consider the buffer proteins to be embedded in the ER membrane, which would be expected to give them a lower diffusivity ($D_b \approx 1\mu m^2/s$ [56]) and leave their motion unaffected by any putative luminal flows. Thus, luminal flows enhance Ca^{2+} release specifically by driving mobile luminal buffer proteins at high Péclet number, with little effect on the free Ca^{2+} ions themselves.

These results highlight the importance of buffer protein mobility for efficient Ca^{2+} delivery. For luminal proteins, this mobility can be further enhanced by super-diffusive motion in the tubules. Notably, the luminal chaperone calreticulin binds Ca^{2+} with high capacity through the many negatively charged residues of its acidic C-terminal domain [40]. However, the closely related membrane protein calnexin has its C-terminal domain situated on the cytosolic side of the ER membrane and thus lacks the ability to provide high-capacity Ca^{2+} storage [57]. Our calculations imply that by relegating Ca^{2+} buffering capacity to mobile luminal proteins, the cell may gain an advantage in the ability to rapidly release Ca^{2+} from local regions of the ER.

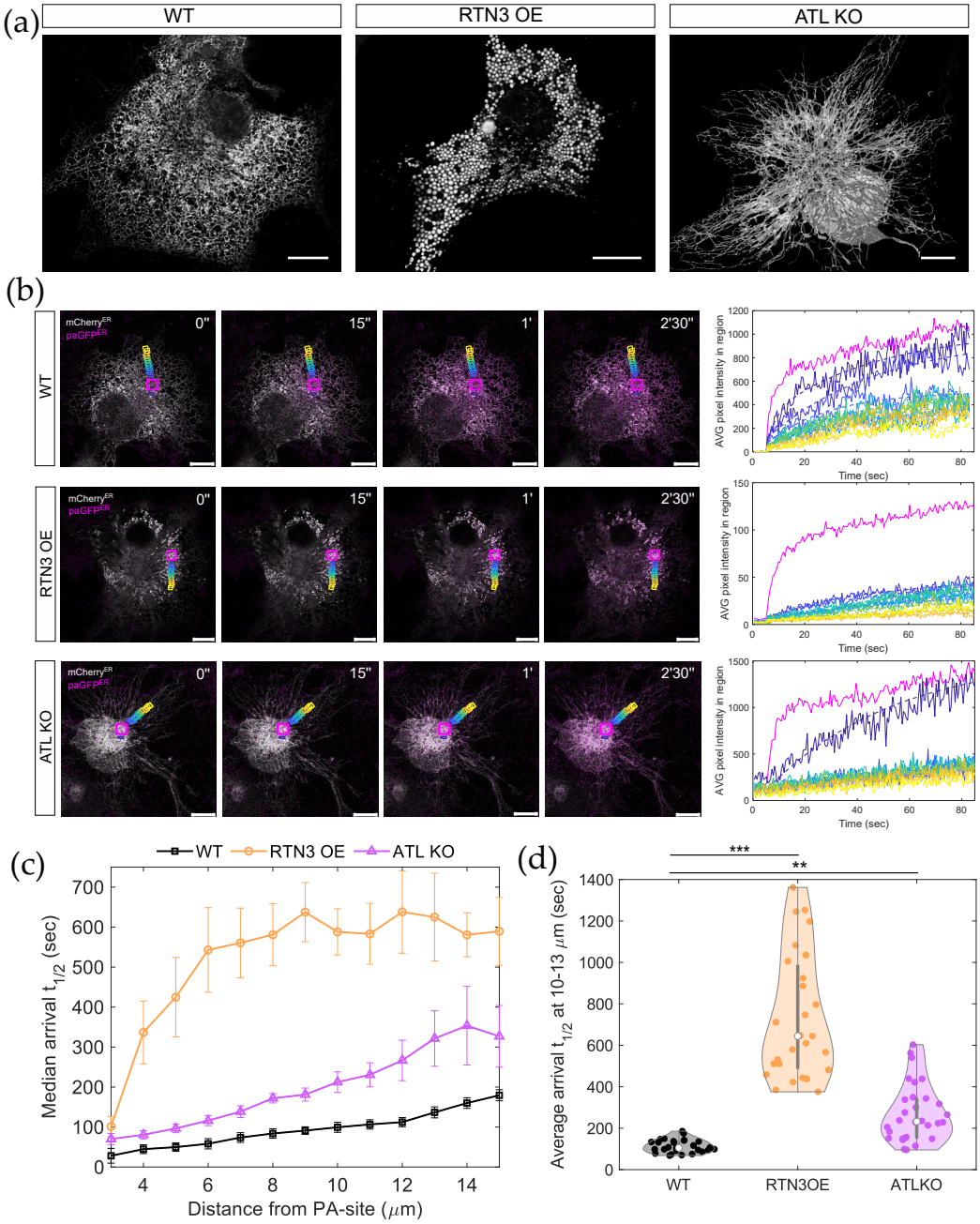

FIG. 3. Reduced transport of luminal proteins in perturbed ER morphologies. (a) Representative image of exogenously expressed ER luminal marker (mCherryER) in live COS-7 cells WT and overexpressing an ER shaping protein reticulon 3 isoform E (RTN3 OE) or double knockout of Atlastin 2 & 3 (ATL dKO). Note the fragmentation of lumen into enlarged, non-reticular structures and reduction in number of junctions along long, unbranched tubules respectively. (b) Photoactivation pulse-chase assay. Illumination of ER-targeted photoactivable GFP ($paGFP^{ER}$) with 405nm laser restores the characteristic fluorescence of conventional GFP. Spatiotemporal spreading of the photoactivated $paGFP^{ER}$ molecules in the ER lumen is monitored while being continuously and locally supplied at photoactivation site (pa-site) in the perinuclear region during image acquisition. ER luminal transport rates are deduced from quantifying the effective half-time for signal rise of the $paGFP^{ER}$ at region of interests placed at increasing distances around the pa-site. Representative merged images of exogenously expressed ER luminal marker (mCherryER) and $paGFP^{ER}$ signal distribution in COS-7 cells with normal ER network (WT), fragmented lumen (RTN3 OE) and unbranched tubules (ATL dKO). Pa-site is represented in magenta together with representative ROIs along one axis around it. Corresponding $paGFP^{ER}$ average (AVG) pixel intensity in those ROIs over time is plotted on the right panel. (c) Median $paGFP^{ER}$ arrival time at respective distances from the pa-site (averaged together over all cells) (d) Average arrival time in ROIs located 10-13μm around pa-site. Each dot represents the arrival times from all ROIs at a specific distance in a single cell, averaged together. [WT: n= 8, RTN3 OE: n=8, ATL dKO: n=14 cells. $^{**}p < 0.01$, $^{***}p < 0.001$, KS test performed on distributions of averages for ROIs located at 10μm.] Scale bars: 10μm.

D. ER structural perturbations reduce luminal connectivity and hinder transport

Our physical model demonstrates that long-range transport of Ca^{2+} ions and mobile buffer proteins through the ER lumen is key to efficient localized Ca^{2+} release. These results highlight a potentially important role for the highly connected morphology of the peripheral ER as an intracellular transport network. A natural empirical test of this theoretical prediction would involve perturbing the ER architecture to limit the connectivity of the peripheral network, and measuring the consequent effect on luminal particle transport. However, the genetic and pharmacalogical toolkit for altering ER structure is limited. We use state-of-the-art manipulations relying on the altered expression of two ER tubule morphogens to affect visible changes in the network.

An extreme change in network connectivity is achieved through overexpression of the tubule-stabilizing protein RTN3e, resulting in the peripheral ER lumen breaking up into poorly connected vesicular structures [58] (Fig. 3a). To quantify the spreading of luminal material through the perturbed ER, we use a previously reported approach of continuous photoactivation followed by spatial chase (CPAC [8]) of ER-targeted photoactivable GFP ($paGFP^{ER}$) from an initial activation region (Fig. 3b). The rate of signal rise is recorded within small regions of interest (ROIs) at different distances from the photoactivation site, and the median time-scale for signal arrival is found to increase with increasing distances (Fig. 3c).

Notably, the eventual arrival of photoactivated luminal proteins in spatially distant ROIs implies that some luminal connectivity is maintained even in the apparently fragmented ER of RTN3 OE cells. However, the arrival times are much longer in RTN3 OE cells as compared to wildtype cells (Fig. 3c,d), where we observe a super-diffusive transport profile for $paGFP^{ER}$ luminal marker as previously shown to be consistent with an active flow model of ER luminal transport [8, 54]. The greatly reduced arrival rates of luminal proteins may be due to slow escape from voluminous ER fragments into narrow tubular connections, or to the constrictions of tubules that serve to partially block luminal continuity between the ER fragments. Such constrictions have previously been reported to arise from overexpression of reticulon proteins [59].

A more moderate alteration to ER connectivity involves manipulating the amount of junctions in the ER tubular network. This is achievable through a double knockout of the junction-forming morphogens Atlastin 1&2 (motor neuron disease-associated ATL2/3), leading to peripheral ER structures with long radially oriented tubules and reduced inter-tubule junctions [60, 61] (Fig. 3a). Analysis of CPAC measurements indicates that luminal content transport is slowed in ATL dKO cells, resulting in higher median half-times of signal arrival to distant regions, as compared to wildtype cells (Fig. 3c,d). This morphological perturbation thus retains the tubular morphology of the peripheral ER while reducing the overall connectivity and hence its efficacy as a transport network.

Given their demonstrated effect on protein transport rates, the manipulations of ER structure by RTN3 overexpression and ATL knockout provide a practical approach for probing the dependence of Ca^{2+} signaling on ER integrity, both *in silico* and in live cells.

E. Reduced ER connectivity is predicted to lower local Ca^{2+} release rates

With the above tools for ER architecture manipulation in mind, we proceed to investigate the extent to which their specific effects on luminal transport kinetics should be expected to alter Ca^{2+} release magnitudes. We generate simplified models of ER structure that incorporate key geometric aspects of the experimental morphogen perturbations.

The model incorporates a large reservoir of luminal volume in a perinuclear ER region, connected to a network structure representing the peripheral ER (Fig. 4a). The complex morphology of the perinuclear ER sheets is not incorporated into the model directly; instead we make the simplifying approximation that the perinuclear reservoir is well-mixed and maintains a spatially uniform concentration. The volume of this reservoir is taken to be commensurate with a single ER sheet of thickness 60nm, surrounding a spherical nucleus 15μm in diameter. We note that over the few-second timescales considered here, the perinuclear region does not empty substantially and its precise volume does not affect the results.

We next consider alternate morphologies of the peripheral ER network, as compared to a honeycomb structure representing wildtype ER (Fig. 4a.i). To represent the partially disconnected ER architecture in cells overexpressing Rtn3, we build a network consisting of small well-mixed bubbles (radius 0.3μm), separated by very narrow tubules of radius 10nm (Fig. 4a.ii). Notably, this structure has a total luminal volume that is 3$\times$ larger than the honeycomb network. We assume that the total quantity of buffer proteins is unchanged and the buffer protein concentration (S) in the enlarged ER is thus reduced by 3$\times$. This assumption rests on the premise that buffer protein production and degradation rates are regulated in a manner that is independent of ER volume. By contrast, we assume the initial free Ca^{2+} concentration remains at 0.5mM, since Ca^{2+} pumps with a fixed driving potential are expected to maintain a fixed luminal free Ca^{2+} concentration [44]. Thus, the total quantity of Ca^{2+} stored in the lumen is increased by only about 40% as a result of the greater ER volume. Empirical measurements supporting these assumptions are discussed in the subsequent section.

When comparing local Ca^{2+} release, we assume that the same number of Ca^{2+}-release channels open in both the honeycomb and the bubbled structure, so the perme-

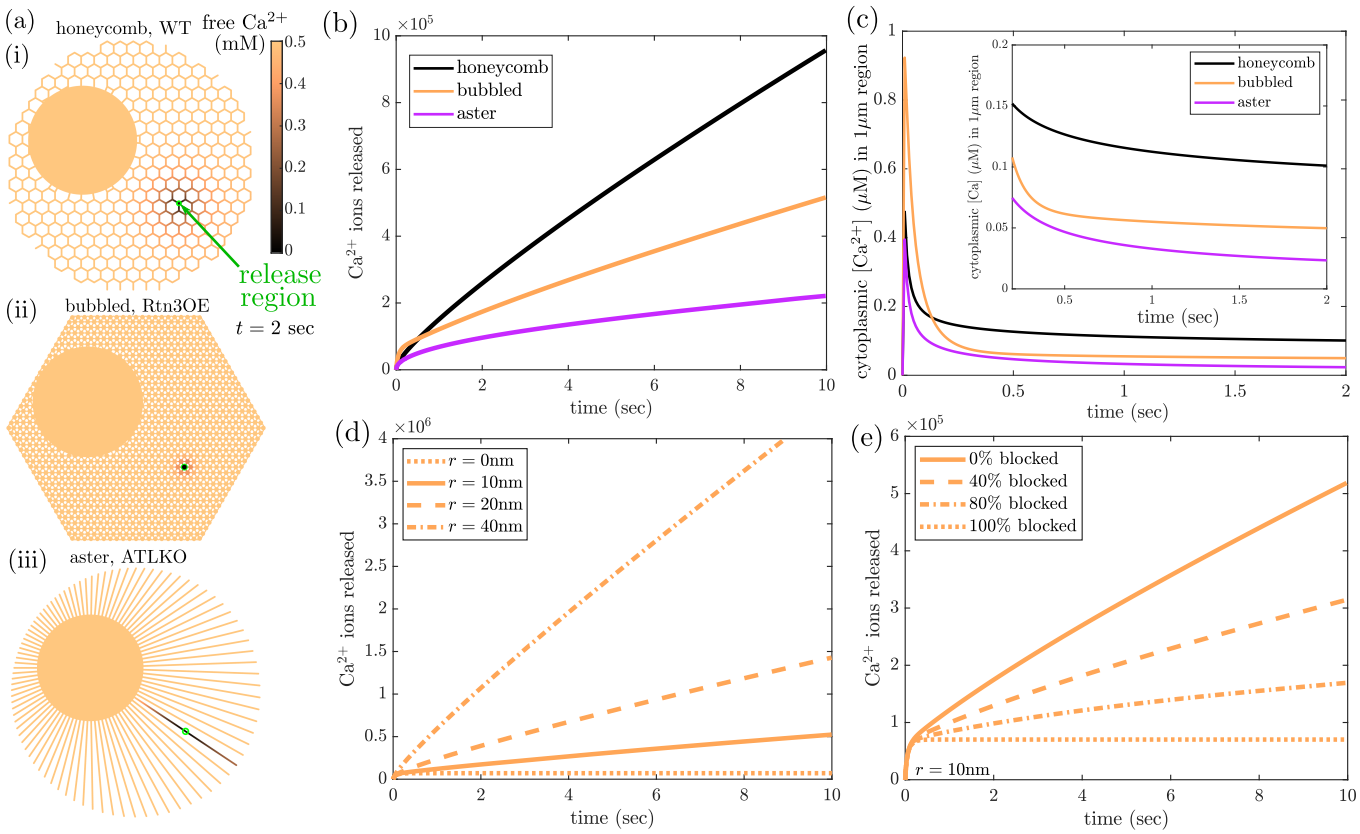

FIG. 4. ER network architecture is predicted to modulate local Ca^{2+} release. (a) Simulation snapshots on idealized network structures, including a well-mixed perinuclear region, representing (i) a well-connected ER network, (ii) a network of bubbles connected by 10nm-radius narrow tubules, (iii) an aster network with long radial tubules. Green circle marks release region. Color shows free Ca^{2+} density at time $t = 2$sec. Permeable surface area, total quantity of buffer proteins, and initial free Ca^{2+} concentration are kept constant between the networks. Parameters are set to $D_b = 3\mu m^2/s$, $K_D = 0.2$mM, $P = 20\mu m/s$, $R \approx 0.3\mu m$. (b) Simulated cumulative Ca^{2+} ions released over time from the network structures shown in (a). (c) Predicted cytoplasmic [Ca^{2+}], averaged over $1\mu m$ region around release site, for same simulation runs as in (b). Inset shows zoom with initial transient bolus excised. (d-e) Effect of reduced connectivity on cumulative Ca^{2+} ions released from bubbled network structure. (d) Different tubule radii. Dotted line: bubbles are disconnected ($r \to 0$). Other lines show networks with bubbles connected by tubules of radius $10nm$ (solid), 20nm (dashed), and 40nm (dash-dotted). (e) Luminal blockages prevent Ca^{2+} and buffer transport across randomly selected tubules. Full tubule connectivity (solid), 40% of tubules blocked (dashed), 80% blocked (dash-dotted), all tubules blocked (dotted). Results are averaged over 10 iterations.

ability of the releasing bubble is set to give the same initial release rate in both structures. Because the volume of the permeable bubble is much higher than the volume of permeable tubules in the local region, the overall short-time release magnitude (< 0.5sec) is greater in the bubbled structure (Fig. 4b). However, the reduced transport through the narrow tubules connecting the bubbles quickly becomes limiting, so that the total amount of Ca^{2+} released over multi-second timescales is lower in the bubbled network. Furthermore, if we model the cytoplasmic Ca^{2+} levels in a region surrounding the local release site (Eq. 7), the predicted Ca^{2+} levels are approximately 2-fold lower compared to the wildtype network (Fig. 4c).

The reduction in Ca^{2+} delivery can be tuned by adjusting the connectivity between neighboring bubbles. For example, wider tubules connecting the bubbles allow for substantially faster Ca^{2+} release (Fig. 4d). Extremely narrow tubules resulting from RTN3e overexpression may also be expected to be subject to sporadic blockages, where closure of the tubule prevents luminal connectivity [59]. As the extent of tubule blockage is unknown, we explored a range of possible blockage probabilities (Fig. 4e), which showed the decrease in Ca^{2+} release as more tubules are blocked. Completely disconnecting the bubbles results in all of the Ca^{2+} being released from the permeable bubble within approximately 0.2sec, followed by no further release.

An alternate model architecture for the peripheral ER comprises a radial structure of long tubules that are connected only at the perinuclear reservoir (Fig. 4a.iii), similar to the ER morphology observed in ATL dKO cells (Fig. 3 a.iii). The tubule density is chosen such that the total volume of the lumen in this structure matches

that of the honeycomb network. The predicted rate of Ca^{2+} release and cytoplasmic Ca^{2+} levels are found to be substantially slower for the radial architecture than for the honeycomb lattice (Fig. 4b,c). This effect can be accounted for by noting that ion delivery to the release region in the radial architecture is effectively one-dimensional. The Ca^{2+} and buffer proteins must diffuse through the one long tubule passing through the permeable zone, and cannot be brought from other tubules without first passing through and then escaping from the large perinuclear reservoir. One-dimensional delivery results in a rapid depletion of the Ca^{2+} load within the tubule (Supplemental Video 2). Thus, the reduced connectivity of this network structure is predicted to limit Ca^{2+} delivery and release.

F. Ca^{2+} release is slowed in perturbed ER morphologies

We next proceed to experimentally quantify local Ca^{2+} release events in COS-7 cells with functional ER Ca^{2+} storage but varying extent of network connectivity, with either no perturbation, or highly disconnected networks in RTN3 OE cells, or mildy reduced network connectivity in ATL dKO cells.

First, we establish the extent to which ER morphological manipulations affect the steady state ER Ca^{2+} concentration and its overall storage capacity (parameters that can influence the magnitude of ER release). To measure ER Ca^{2+} in absolute terms we used a FRET reporter with a relatively low K_d tuned to the luminal high Ca^{2+} environment [62], read out by fluorescence lifetime imaging (FLIM). We improved its optical properties to extend the accuracy in calibrated FLIM-based mesurements, by optimizing the photophysical characteristics of the FRET donor/acceptor (mTurquoise with a single lifetime and REACH with low emission, Fig. 5a; see Methods for details). The dynamic range of the new probe is well adapted to detect physiological variations in ER Ca^{2+} concentration ($[Ca^{2+}]_{ER}$) after calibration in maximal and minimal Ca^{2+} conditions. Measurements in COS-7 WT confirm the baseline value $[Ca^{2+}]_{ER} = 0.47 \pm 0.11$ mM (Fig. 5b, c). The structurally perturbed ER retained its Ca^{2+} storage characteristics: free Ca2+ concentrations were 0.59±0.19 mM and 0.62±0.16 mM in cells with tubular junction loss (COS-7 ATL dKO) and in the fragmented ER (COS-7 RTN3 OE), respectively. The latter structure may accommodate slightly higher amounts of free Ca^{2+} due to an increase in volume. Our quantitative model indicates that these small increases in free Ca^{2+} levels are not expected to have a substantial effect on the amount of Ca^{2+} released (Supplemental Fig. S5).

Further, the total ER Ca^{2+} load appears not significantly altered in cells with fragmented (RTN3 OE) or radial (ATL dKO) ER architecture compared to COS-7 WT, as evident from quantifying the total release elicited by thapsigargin (a SERCA pump inhibitor that globally releases free and buffer-bound ER Ca^{2+}; Fig. 5d, e). This is consistent with our model, which predicts only a small to moderate increase in total Ca^{2+} load within the bubbled network (ranging from $12 - 40\%$, depending on the assumed size of the bubbles; see Supplemental Fig. S5). Thus, the membrane components regulating Ca^{2+} content in the ER (Ca^{2+} pumps and channels [63]) appear to not be significantly impaired by ER morphological changes and effectively prevent the depletion or overload of its Ca^{2+} storage. The live-cell measurements therefore justify our model assumptions that ER morphological perturbation does not reduce either the free or the total Ca^{2+} load in the ER lumen.

Since networks with perturbed connectivity retain similar baseline levels of Ca^{2+} compared to the normally shaped network, we next evaluate their ability to supply Ca^{2+} in spatially restricted regions. To generate localized Ca^{2+} releases, we use photoactivated IP3 uncaging to deliver controlled amounts of IP3 by modulating exposure time and intensity of a 405nm laser. This triggers sporadic opening of IP3R Ca^{2+} channels and generation of localized Ca^{2+} release events comparable to Ca^{2+} 'puffs'. Ca^{2+} release events are monitored in the cytoplasm by measuring intensity changes of an ER membrane-tethered cytosolic Ca^{2+} sensor (GCaMP3-ER). ROIs with individual release events restricted in space and time are detected semi-automatically (Fig. 5f, details in Methods). Each release event corresponds to a defined peak in the local Ca^{2+} signal. This peak is expected to be limited by a combination of several factors: the Ca^{2+} release rate from the ER, the dilution of Ca^{2+} in the cytoplasm, and the chelation and clearance of cytoplasmic Ca^{2+}. We thus do not aim to quantitatively compare peak magnitudes with model predictions, but rather to qualitatively note the difference in peaks between cells with differing ER structures.

Before inducing local releases, we confirm that IP3R machinery is functional in all cell types despite ER morphology perturbations. We successfully trigger global Ca^{2+} release through CICR [5] upon uncaging high amounts of IP3 with long laser exposure times (30s). We then induce local Ca^{2+} transients and estimate the overall extent of release by taking the area under the curve of each transient Ca^{2+} peak. On average, the peak integrals are found to be significantly lower in RTN3 OE cells, suggesting that their poorly connected ER structures reduced the ability to release high amounts of Ca^{2+} in localized regions along the ER (Fig. 5g). Similarly, the peak integrals are reduced for ATL dKO cells, where the ER exhibits long tubules and reduced junctions. Although Ca^{2+} release rates cannot be extracted directly from the peak integrals, the reduction in total signal during each transient event is consistent with a slowing of Ca^{2+} release rates.

These measurements are in line with our model prediction that dense ER tubule connectivity is necessary to support efficient local Ca^{2+} release through transport

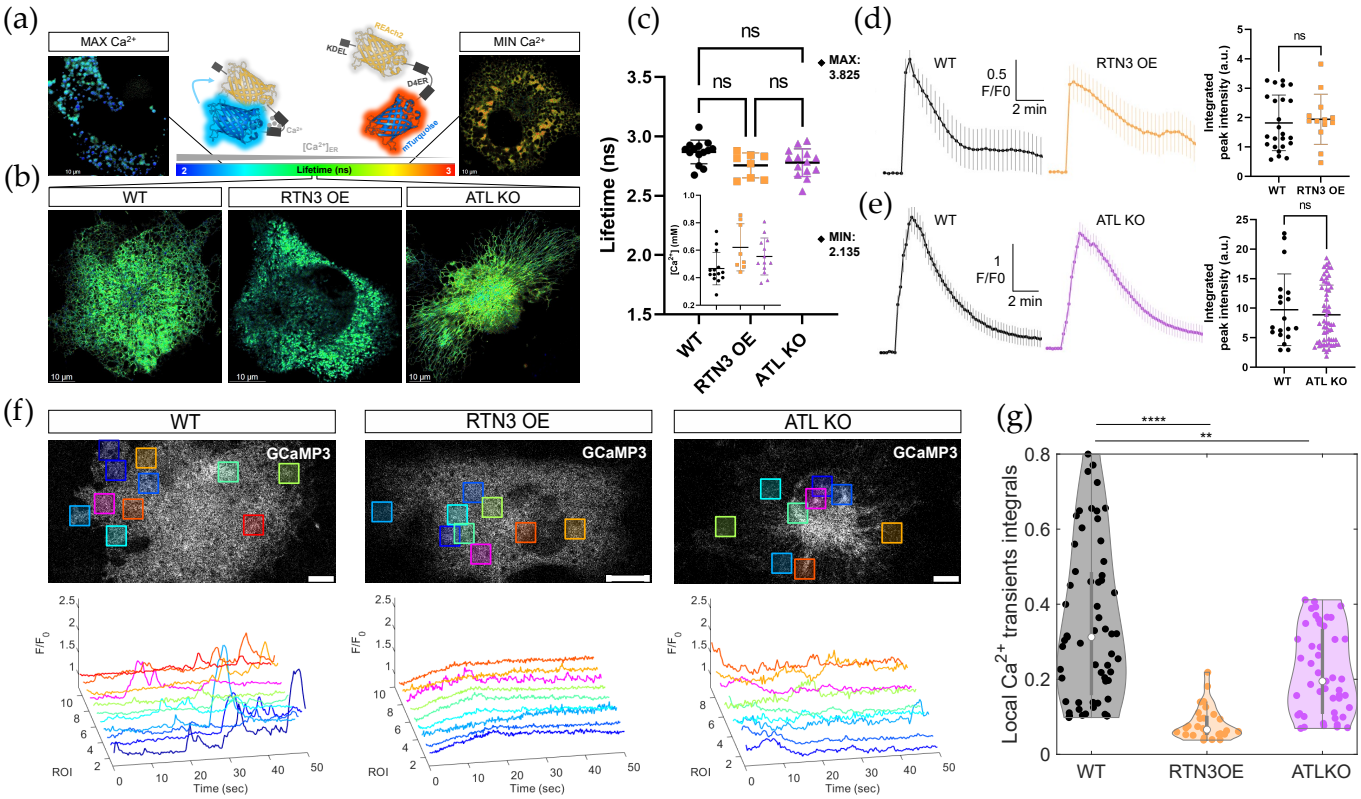

FIG. 5. Perturbation of ER architecture hinders localized Ca^{2+} transients without affecting Ca^{2+} storage. (a) (center) Schematic of FLIM method for measuring absolute Ca^{2+} concentration; ER-targeted D4ER-Tq FRET Ca^{2+} probe with new fluorophores is drawn bound/unbound to Ca^{2+} (high/low FRET respectively) with corresponding mTurquoise's lifetimes. KDEL: ER retention motif. Representative FLIM images for calibration, showing extreme luminal Ca^{2+} levels with (left) maximal Ca^{2+} obtained by ionomycin (10μM) treatment and (right) minimal Ca^{2+} obtained by thapsigargin (3μM) treatment. (b) Representative FLIM images in COS-7 cells with altered ER network structure corresponding to WT, RTN3 OE and ATL dKO. (c) Quantitative FLIM measurements of luminal Ca^{2+} concentration (each data point represents one cell). Mean $[Ca^{2+}]_{ER}$ is not significantly changed between conditions. Mean lifetimes in maximal and minimal Ca^{2+} conditions are indicated. (WT: n=14, RTN3 OE: n=8, ATL dKO: n=14; ns: $p > 0.05$, 1-way ANOVA). (d-e) Measurement of total ER Ca^{2+} load by global depletion. Cytosolic Ca^{2+} fluorescence intensity is plotted over time after addition of thapsigargin (1μM). Integrated fluorescence intensity is not significantly changed between conditions. Probes used were (d) Oregon Green BAPTA-1, AM for WT/RTN3 OE (WT: n=24, RTN3 OE: n=13, ns: $p > 0.05$, KS test) and (e) GCaMP3-ER for WT/ATL dKO (WT: n=19, ATL dKO: n=59. ns: $p > 0.05$, KS test). (f) Representative fluorescence intensity images of GCaMP3-ER probe for cytoplasmic Ca^{2+} released from the ER in COS-7 WT, RTN3 OE and ATL dKO cells after light-induced IP3 uncaging. Semi-automatically detected ROIs around local Ca^{2+} transients are represented as colored squares and corresponding signal intensity traces over time within each ROI are plotted. (g) Quantification of integrated fluorescence intensity under each peak during local Ca^{2+} transients (each data point represents one local Ca^{2+} transient from WT: n=11, RTN3 OE: n=8, ATL dKO: n=17 cells. $^{****}p < 0.0001$, $^{**}p < 0.01$, KS test).

of Ca^{2+} and buffer proteins from neighboring regions of the network. Perturbations to this connectivity through altered expression of ER morphogens is shown to alter the magnitude of local Ca^{2+} release events. The theory and experiments thus both provide insight into a potentially important functional role of the highly connected ER network morphology.

IV. DISCUSSION

The physics-based modeling of this study demonstrates that localized Ca^{2+} events rely on Ca^{2+} transport through a well-connected ER lumen, with the aid of mobile buffer proteins. Furthermore, live-cell imaging together with manipulations of ER morphogen expression show that alterations to ER structure both hinder transport through the network and decrease the magnitude of local Ca^{2+} signals.

Raising the local cytoplasmic Ca^{2+} level requires first a one-dimensional ER tubule, then an effectively two-

dimensional network, to supply sufficient Ca^{2+} to overcome rapid three-dimensional dilution. This functional necessity is achieved by storing a high luminal Ca^{2+} load, primarily bound to high-capacity buffer proteins. Our simulations show that transport through the network results in a very slow depletion of free luminal Ca^{2+} in the release region, giving rise to an optimum intermediate binding strength ($K_D \approx 0.2$mM) for the most rapid Ca^{2+} release over a broad range of timescales ($0.1 - 10$ sec). This moderate binding strength matches some estimates of the high-capacity sites of calreticulin, a major Ca^{2+}-storing luminal buffer protein [53]. In addition, our model demonstrates that Ca^{2+} release is enhanced by the mobility of the buffer proteins, particularly in the presence of putative active flows within the ER lumen. This feature may explain why the luminal chaperone calreticulin is responsible for carrying much of the intra-ER Ca^{2+} load on its many Ca^{2+}-binding sites, while its membrane-bound analogue calnexin lacks a high-capacity Ca^{2+}-storage domain [57].

Importantly, our results highlight a key structure–function relationship of the peripheral ER network. The interconnected lattice of ER tubules forms a topologically sequestered domain filled with excess Ca^{2+} in proximity to all cellular regions. Efficient transport through the network allows Ca^{2+} to be rapidly delivered and released anywhere within the cell. We perturb the ER architecture by altering morphogen expression levels, yielding structures with extended tubules (ATL dKO) and partially fragmented ER (RTN3 OE). Measurements of photoactivated protein spreading demonstrate that both these structural perturbations result in slower long-range transport through the ER lumen. Our simplified physical model of Ca^{2+} transport predicts decreased rates of Ca^{2+} release in both these altered morphologies. Furthermore, measurements of local Ca^{2+} events magnitudes show that indeed releases are much smaller in the cells with long-tubule or fragmented ER as compared to the wild-type cells, with their well-connected lattice-like network architecture.

While it is possible that other effects of the ER morphogen perturbations are responsible for the reduced Ca^{2+} release, our additional measurements help eliminate some of these alternate explanations. In particular, the fluorescence lifetime measurements show that free Ca^{2+} concentration in the perturbed ER lumen is similar to or even higher than the wildtype cells. Additionally, measuring cytoplasmic Ca^{2+} levels following global release indicates that the total luminal Ca^{2+} load is similar in ATL dKO and RTN3 OE cells as compared to wildtype. Thus, there is no decrease in luminal Ca^{2+} availability to account for the reduced magnitudes of localized Ca^{2+} events. Other alternate explanations, such as a decrease in IP3R channel density or opening sensitivity would require both unrelated perturbations to lead to the same unintended effect. Given that the two very different morphological changes both have in common a demonstrated reduction in ER luminal transport, the most parsimonious explanation is that this reduced transport is responsible for the decreased magnitude of local Ca^{2+} releases, consistent with our model predictions.

In this study, cultured COS-7 cells were employed due to their easily visualized extended ER network, and their tractability as a model system for ER morphogen perturbations. However, the key conceptual results of intraluminal Ca^{2+} and buffer transport supporting localized release, also apply to more specialized cell types. Neuronal cells, in particular, exhibit highly extended ER architectures that provide a continuous Ca^{2+} store linking the cell body to the distal tips of long and/or branched projections [26]. In photoreceptor cells luminal transport from the somatic ER has been shown to replenish Ca^{2+} stores in distal termini [65]. Perturbations of the ER morphogen Rtn4/Nogo in neuronal cells have been found to modulate axonal regeneration [66, 67] as well as alter Ca^{2+} release [8]. Our results demonstrate the need to consider both buffer protein and free ion transport through the extended ER structures of neurons, as well as the importance of robust luminal connectivity. Expansion of the model and live-cell measurements of intra-ER transport to a variety of specialized ER architectures of relevance to neuronal cells forms a potentially fruitful future expansion of the current work.

In many cellular contexts, localized Ca^{2+} release events (puffs, sparks, or twinkles) play an important biological role in providing the initial trigger for the large-scale signaling waves propagated by Ca^{2+}-induced Ca^{2+} release [5]. In some cells, frequent localized release events are themselves responsible for functional regulation, as in gliotransmitter release by astrocytes [68]. The connection between ER morphology, luminal transport, and Ca^{2+} delivery thus forms a globally important structure-function link at the cellular scale. The intertwined physical modeling and live-cell imaging approaches demonstrated in this work have potentially broad applicability for elucidating the importance of ER architecture in a variety of cellular systems.

V. MATERIALS AND METHODS

A. Model for Ca^{2+} buffering and transport

In modeling Ca^{2+} release, we consider both free and buffer-associated Ca^{2+} within the ER lumen. The on- and off-rates of ions from the buffer binding sites are assumed to be very fast, so that the free and bound Ca^{2+} concentrations are always taken to be equilibrated. Defining U as the free Ca^{2+} concentration, B as the bound Ca^{2+} concentration, S as the total concentration of binding sites, and K_D as the dissociation constant for each binding site, gives the equilibrium relation

$$K_D = \frac{U(S-B)}{B}. \tag{3}$$

The total Ca^{2+} concentration $C = U + B$ is then

$$C = U + \frac{US}{U + K_D}. \tag{4}$$

Ca^{2+} release is modeled as occuring in a localized region, containing a total length L of ER tubules with an effective membrane permeability P setting the rate of release for free Ca^{2+} ions. The parameters for our models are summarized in Table I.

1. *Release of local Ca^{2+} pool in model without transport*

The simplest model is one where the permeable region is completely independent of the rest of the network, and only Ca^{2+} ions within that region can be released. For simplicity, we make the assumption that the permeable region is well-mixed, with no transport processes involved except for the movement of Ca^{2+} ions across the membrane. In this case, we can write the rate of change in luminal Ca^{2+} as

$$\frac{dC}{dt} = -\frac{PA_{\mathrm{ER}}}{V_{\mathrm{ER}}}U = -\frac{2P}{r}U, \tag{5}$$

where r is the radius of ER tubules, $A_{\mathrm{ER}} = 2\pi rL$ is the surface area of the permeable tubules, and $V_{\mathrm{ER}} = \pi r^2 L$ is their volume. Plugging in Eq. 4 gives the time-evolution of the free Ca^{2+} concentration, as in Eq. 1. The time evolution of luminal free Ca^{2+} is found by integrating Eq. 1. The current of Ca^{2+} out of the ER lumen is then given by

$$J(t) = PA_{\mathrm{ER}}U(t). \tag{6}$$

To estimate the permeability of the ER within the release region (total tubule length $L = 3R$), we note that measurements of Ca^{2+} puffs in oocytes indicate a typical peak current of approximately $I \approx 0.4$pA [28]. Assuming only local Ca^{2+} is released at very short times, Eq. 6 gives an estimate of the corresponding permeability as $P = J/(2\pi rLU_0) \approx 20\mu$m/s.

To model the local cytoplasmic Ca^{2+} levels, we approximate all the Ca^{2+} release as occuring at a single-point, assume the Ca^{2+} ions spread from this source with diffusivity D_{cyto}, and average the resulting concentration profile over a sphere of radius $R_{\mathrm{loc}} = 1\mu$m. This averaged local cytoplasmic concentration is given by:

$$\psi(t) = \frac{3}{R_{\mathrm{loc}}^3}\int_0^t dt' \int_0^{R_{\mathrm{loc}}} dr\ r^2 G(r, t-t')J(t) \tag{7}$$

where $G(r,t) = (4\pi D_{\mathrm{cyto}}t)^{-3/2}e^{-r^2/(4D_{\mathrm{cyto}}t)}$ is the Green's function for three-dimensional diffusion.

In addition to this simple estimate of cytoplasmic free Ca^{2+}, in the Supplemental Material we numerically solve a model that takes into account equilibrated binding of Ca^{2+} ions to diffusive cytoplasmic buffer proteins.

B. Network structures

The honeycomb network in Fig. 1 and 2 serves as a simplified representation of a wild-type ER structure. The structure consists of a circle of radius 25μm (representing the cell) excised from a periodic honeycomb network with edges of length 1μm connecting degree-3 nodes. So long as the permeable region is far from the network boundary, the spatial extent of the network does not have a substantial effect on local Ca^{2+} release.

To explore the effect of network structure, we first construct an alternate 'wild-type' honeycomb network that includes a well-mixed perinuclear reservoir. This reservoir represents the entire perinuclear ER as a flat sheet with surface area and volume corresponding to a spherical shell of diameter $2R_{\mathrm{nuc}} = 15\mu$m and thickness $h = 60$nm. We do not consider transport within the perinuclear region, treating it as a single reservoir with spatially uniform concentration fields. We note that in the lattice-like network structures (Fig. 4a.i,ii), the presence of this reservoir does not noticeably affect any results since the depletion in the luminal Ca^{2+} does not extend that far from the permeable region during the few-second timescales considered.

To represent the partially fragmented ER observed in RTN3 OE cells, we create a network structure consisting of spherical reservoirs of radius $R_{\mathrm{bub}} = 0.29\mu$m, packed in a hexagonal lattice with nearest-neighbor center-to-center distance $\ell_{\mathrm{sep}} = 0.85$nm. These parameters were extracted from the image in Fig. 4 by detecting individual bubble-like fragments using TrackMate [70]. We assume full connectivity between nearest-neighbor bubbles, via tubes of radius $r = 10$nm. A single bubble is selected to be permeable, and its permeability is set such that the initial flux of Ca^{2+} from the bubble is equal to the initial flux out of a permeable region of radius $R = 0.29\mu$m in the corresponding wild-type control (honeycomb network). The total luminal volume of the modeled ER in the bubbled network is approximately 3-fold higher than the luminal volume in the wild-type control. We implement the assumption that the total quantity of buffer proteins remains unchanged by decreasing the initial buffer protein concentration from 0.1mM (wild-type control) to 0.03mM.

To represent the long-tube ER observed in ATL dKO cells, we create an 'aster' network consisting of individual tubules stretching from the edge of the perinuclear region to the boundary of the circular domain. Each tubule has radius $r = 50$nm and a total of $n = 91$ tubules is included to give approximately the same total tubule length (and hence same luminal volume) as the wild-type honeycomb network. The release region is set to a radius of $R = 0.4\mu$m, giving approximately the same initial release rate as in the wild-type network.

TABLE I. Default parameters for model of luminal Ca^{2+} dynamics

Parameter	Description	Value	Reference
U_0	initial free [Ca^{2+}]	0.5 mM	[42–44]
S	concentration of luminal buffer binding sites	2.7 mM	[41] (500μg/g cell vol)
D_b	buffer protein luminal diffusivity	2.8μm^2/s	[8]
D_{Ca}	free Ca^{2+} luminal diffusivity	28μm^2/s	set to $10 \times D_b$
D_{cyto}	cytoplasmic Ca^{2+} diffusivity	200μm^2/s	[69]
r	ER tubule radius	50μm	[51]
R	spatial extent of local release region	0.25μm	[28]
P	permeability of local release region	20μm/s	[28] (0.4pA peak current)
R_{loc}	radius of region for averaging cytoplasmic Ca^{2+}	1μm	
v	flow velocity	20μm/s	[54]

C. Numerical implementation of spatiotemporal dynamics on a network

To incorporate the transport of Ca^{2+} through the ER, we use a numerical finite volume method [71] to evolve forward in time the concentration of free Ca^{2+} ions and buffer sites on a network. Binding of Ca^{2+} to the buffer sites is assumed to be equilibrated everywhere. The finite volume simulations are implemented in Fortran 90 and the source code is provided at `https://github.com/lenafabr/networkSpreadFVM`.

1. *Finite volume method on tubular network*

The network structure is meshed into cells of length Δl (maximum length 0.1μm). Each cell either represents a segment of network tubule or a triskelion of tubules centered around a three-way junction. The network topology defines the boundaries between mesh cells. All mesh cells whose center falls within radius $R = 0.25\mu$m of the network center are labeled as permeable. The surface area of each mesh cell is set to $A_i = 2\pi r \Delta l$ and its volume to $V_i = \pi r^2 \Delta l$, where r is the tubule radius.

The state of the network is defined by two field variables: $U_i(t)$ represents the concentration of free Ca^{2+} in mesh cell i, and $S_i(t)$ represents the total concentration of buffer sites in mesh cell i. Initial conditions are set to spatially constant concentrations $S_i(0) = 0.1$mM (by default) and $U_i(0) = U_0 = 0.5$mM. We note that in the case of purely diffusive transport, $S_i(t)$ remains constant for all mesh cells, but in the presence of flows it is also be evolved in accordance with the dynamic equations (Eq. 2). The total Ca^{2+} concentration in a mesh cell ($C_i(t)$) is set at each step using Eq. 4.

At each timestep, we compute the change in total Ca^{2+} (ΔC_i) and total binding sites (ΔS_i) on each mesh cell, using standard finite-volume methods [71] to find the diffusive flux (via a vertex-centered difference scheme, detailed below) and advective flux (via a Lax-Wendroff scheme [71]) into or out of each mesh cell, in accordance with Eq. 2. Terminal edges of a mesh cell are taken to be no-flux boundaries. The change in total Ca^{2+} due to leakage from each permeable cell includes an additional term $\Delta C_{\mathrm{i,leak}} = -PA_iU_i\Delta t/V_i$. The current out of the network is given by $J(t) = -\sum_i V_i \frac{\Delta C_{\mathrm{i,leak}}}{\Delta t}$, with the summation over all permeable mesh cells.

From the equilibration constraint (Eq. 4), we find the change in free Ca^{2+} at each time-step, according to:

$$\Delta U_i = \frac{\Delta C_i - U_i \Delta S_i/(U_i + K_D)}{1 + S_i K_D/(U_i + K_D)^2} \tag{8}$$

The concentration fields are then propagated forward in small time-steps $\Delta t = 2 \times 10^{-5}$s for purely diffusive transport and $\Delta t = 10^{-6}$s in the presence of flows. The current out of the network at each time-step is integrated over time to find total Ca^{2+} released, or plugged into Eq. 7 to compute the cytoplasmic Ca^{2+} level.

For active network simulations, flow velocities of magnitude $|v| = 20\mu$m/s are defined in a randomly chosen direction on each edge along the network. After each time step, the velocity along each edge flips direction with probability $1 - \exp(-\Delta t/\tau)$. Because each non-terminal mesh-cell boundary is placed along a network edge, the velocity across each boundary is uniquely defined and is used in the Lax-Wendroff calculation of the advective flux.

2. *Diffusive flux with large well-mixed reservoirs*

For two mesh cells representing neighboring segments of tubule, the diffusive flux along the boundary between them can be written in the standard form:

$$\mathcal{F}^{(U)}_{i+1/2} = -D_{\mathrm{Ca}} \frac{U_{i+1} - U_i}{\ell_{i+}} \tag{9}$$

where $\ell_{i+} = (\Delta l_i + \Delta l_{i+1})/2$ is the separation between mesh cell centers. An analogous expression can be written for $\mathcal{F}^{(B)}_{i+1/2}$ corresponding to the flux of bound Ca^{2+} (defined as $B_i = C_i - U_i$), with D_{Ca} replaced by D_b. The

change in Ca^{2+} concentration due to diffusive transport is then given by:

$$\frac{\Delta C_{i,\text{diff}}}{\Delta t} = \frac{\pi r^2}{V_i}\left(\mathcal{F}^{(U)}_{i+1/2} - \mathcal{F}^{(U)}_{i-1/2} + \mathcal{F}^{(B)}_{i+1/2} - \mathcal{F}^{(B)}_{i-1/2}\right). \tag{10}$$

For the case where one of the mesh cells represents a large well-mixed reservoir, the expression for the diffusive flux must be altered to account for the narrow escape process of diffusive particles leaving the reservoir through small tubule entrances. We consider two types of reservoirs. The perinuclear region is treated as a flat sheet (disc) with surface area $A_{\text{nuc}} = 4\pi R^2_{\text{nuc}}$ and volume $V_{\text{nuc}} = 4\pi R^2_{\text{nuc}} h$, where $2R_{\text{nuc}} = 15\mu$m is the diameter of the nucleus and $h = 0.06\mu$m is the height of a single ER sheet. This approximates the complex perinuclear structure as a single sheet surrounding a spherical nucleus. For the network structure representing fragmented ER in RTN3 OE cells, the bubbles are treated as spheres with surface area $A_{\text{bub}} = 4\pi R^2_{\text{bub}}$ and volume $V_{\text{bub}} = \frac{4}{3}\pi R^3_{\text{bub}}$, for radius $R_{\text{bub}} = 0.29\mu$m.

For a spherical reservoir connected to a narrow tubule of radius r, we consider the steady state flux from the sphere into the tubule, where we assume the concentration throughout the sphere is U_{bub} and the concentration in the tubular mesh cell at a distance $\Delta l_i/2$ from the sphere is U_i. Defining $\tilde{U}_i$ as the concentration at the sphere-tubule junction point, the current out of the sphere must be $I_{\text{bub}} = 4Dr(U_{\text{bub}} - \tilde{U}_i)$ [36]. The current from the tube into the sphere is $I_{\text{tube}} = D\pi r^2(\tilde{U}_i - U_i)/(\Delta l_i/2)$. Setting these two expressions equal to each other at steady-state gives the flux across the boundary between the two mesh cells as:

$$\mathcal{F}^{(U)}_{\text{bub},i} = \frac{4D(U_{\text{bub}} - U_i)}{\pi r + 2\Delta l_i}. \tag{11}$$

This flux expression can be put in the same form as the boundary between two tubular cells (Eq. 9), if we take the reservoir to have an effective length $\Delta l_{\text{bub}} = \pi r/2$. This effective length does not depend on the size of the sphere, because diffusive transport to a narrow target in 3D is non-compact [72] and the current of escaping particles is thus independent of the shape of the confining domain.

To propagate forward the concentration fields in the spherical reservoir, we use an expression analogous to Eq. 10, using the reservoir volume V_{bub}, and incorporating flux across all boundaries to connected tubules.

A similar approach is taken for the disc-shaped reservoir used to represent the perinuclear region. The current out of the sheet through a narrow exit boundary is given by $I_{\text{nuc}} = 2\pi Dh(U_{\text{nuc}} - \tilde{U}_i)/\ln(\hat{R}_{\text{nuc}}/r)$, where $\hat{R}_{\text{nuc}} = \sqrt{A_{\text{nuc}}/\pi}$ is the effective radius of the reservoir [73]. The approximate disc size $\hat{R}_{\text{nuc}}$ assumes that the rate of diffusive escape from the perinuclear sheet is roughly equivalent to escape from a flat disc with the same surface area.

Setting I_{nuc} equal to the current from the tube into the reservoir (I_{tube}) gives the flux across the boundary as:

$$\mathcal{F}^{(U)}_{\text{nuc},i} = \frac{2D(U_{\text{nuc}} - U_i)}{\frac{r^2}{h}\ln(\hat{R}/r) + \Delta l_i}. \tag{12}$$

This expression is analogous to that between two tubular mesh elements, with the effective length of the reservoir set to $\Delta l_{\text{nuc}} = r^2/h\ln(\hat{R}/r)$. The change in reservoir concentration is propagated forward as before, using the appropriate volume V_{nuc} and incorporating flux through the boundaries with all connected tubules.

D. Cell culture, transfections and constructs and reagents

COS-7 (RRID:CVCL_0224) cells were cultured in Dulbeccos modified Eagles medium (DMEM) supplemented with 10% fetal bovine serum (FBS), 2 mM L-Glutamine and 100 U/mL Penicillin-Streptomycin (P/S). Cells were transfected using the Neon Transfection System (Invitrogen) with 2 pulses of 20ms at 900V. RTN3 OE cells were obtained by transfecting COS-7 cells with RTN3-HaloTag plasmid monitored by labelling with JF646; ATL2/3 KO cells were obtained from Junjie Hu (University of Chinese Academy of Sciences).

Caged-IP3 (ci-IP3/PM, #6210) was obtained from Tocris. Thapsigargin (10522-1 mg-CAY) was obtained from Cambridge Bioscience (Cambridge, UK). Janelia Fluor 646-conjugated HaloTag ligand (JF646, not photoactivatable, GA1120) were obtained from Promega (Madison, WI, USA).

E. Continuous photoactivation chase (CPAC)

1. *Image acquisition*

This assay was performed as previously described in [8]. Briefly, COS-7 cells were transfected with paGFP^{ER} plasmid and mCherry^{ER} plasmids (together with RTN3-HaloTag plasmid for RTN3 OE cell line) and 48h post-transfection, cells were taken to microscopy. We used a confocal microscope (STELLARIS8, Leica, Wetzlar, Germany) with a controlled environment (37°C, 5% CO_2) and the following parameters: excitation/emission of 489 nm/495−550 nm for paGFP^{ER} and 567 nm/608−635 nm emission for mCherry^{ER}, frame size of 512 × 512 pixels, scan speed of 1000 Hz, 1.92 frames per second.

Image acquisition series consisted of pre-photoactivation images (10 frames), photoactivation illumination (405 nm, 100% laser power) introduced in a region of interest (photoactivation spot of 5μm × 5μm) for a duration of at least 300 frames (520 ms/frame), using the Fly mode (enabling simultaneous photoactivation and image recording) in the FRAP wizard. Image series were then analyzed semi-automatically as described in the following section.

2. Image analysis

paGFP^{ER} mobility in the ER lumen was determined by photoactivation image analysis and median rise-time estimation using a custom code written in Matlab (version 9.5.0, R2018b, Natick, Massachusetts: The MathWorks Inc.), as previously described in [8]. Briefly, the images of ER luminal marker mCherry^{ER} were used to segment the cell and nucleus shapes manually. The resulting ROI consisted of the area within cell boundary except for the nucleus (eroded by 1 micron to avoid edge effects). The photoactivation region was manually segmented from images of paGFP^{ER} focused on the activation spot during the photoactivation phase and removed from the cell ROI to be analyzed (with a 1μm buffer). Concentric ring regions of width 2 μm were defined around the photoactivation center (centroid of the photoactivation region), starting at 1 μm intervals in distance from it, and sub-divided into wedge-shaped ROIs of arc length 2 μm, shifted by 1 μm around the circle. Wedge ROIs presenting less than 2 μm^2 of valid area after intersection with the segmented cell area were not retained for analysis.

Fluorescence intensity time traces were obtained from every wedge-shaped ROI and normalized by the ROI area. The intensity time series were all fit to adouble-exponential function beginning after the photoactivation start and rising from the pre-photoactivation value to a maximum value set by the final fluorescence of the photoactivated region (assuming that fluorescence in the whole cell will equilibrate to this value at infinite time). The exponential fits served to compute half-time for the signal rise, unless signal-to-noise ratio was insufficient (signal range less than twice the pre-photoactivation standard deviation) or resulting half-time was more than 10 times the recorded timespan. Median arrival $t_{1/2}$ corresponds to the median half-time of all remaining wedge regions at a given radius from the photoactivation center, over all cells in each dataset. The error bars (standard deviation of the median) were obtained by bootstrapping individual cells from each dataset and repeating the analysis to indicate cell-to-cell variation in each reported half-time.

The code for analysing CPAC measurements is available on `https://github.com/lenafabr/photoActivationAnalysis.git`

F. Fluorescence Lifetime Imaging Microscopy (FLIM)

To measure $[Ca^{2+}]_{ER}$, we used Fluorescence Lifetime Imaging Microscopy (FLIM) and a probe inspired from D4ER FRET-FLIM based probe (ECFP/Citrine pair [62]). We improved this probe by swapping the donor fluorophore ECFP to mTurquoise and acceptor Citrine to REAch2. These modifications were expected to provide more accurate $[Ca^{2+}]_{ER}$ estimations as mTurquoise decay can reliably be fitted with a monoexponential as opposed to ECFP and REAch2 is a dark acceptor (nonfluorescent yellow fluorescent protein (YFP) mutant). We performed a calibration of the new version of D4ER, named D4ER-Tq, by inducing maximum Ca^{2+} condition with addition of ionomycin (10μM) and minimal Ca^{2+} condition was obtained by adding thapsigargin (3μM) to trigger full depletion of the Ca^{2+} stored in the ER. The dynamic range of this new version of D4ER was increased from 0.8ns to 1ns. This maximal and minimal values were used to convert lifetimes to Ca^{2+} concentrations. COS-7 cells (WT, RTN3 OE monitored by labelling with JF646, ATL2/3 KO lines) were transfected to express D4ER-Tq probe and 48h post-transfection, cells were taken to microscopy. We used a confocal microscope (STELLARIS8, Leica, Wetzlar, Germany) with a controlled environment (37°C, 5% CO_2) and the following FLIM parameters: excitation/emission of $440/450-500$ nm, pulsed wight light laser at 80 MHz, HyDX detector in counting mode, frame size of 512×512 pixels, scan speed of 400 Hz, and settings were set to reach 5000 photons/pixel. Images were processed using Leica STELLARIS8 FLIM wizard. ROIs were drawn around individual cells and data fitted to a monoexponential decay function. Lifetime values were converted to $[Ca^{2+}]_{ER}$ using the following formula, with D4ER Kd (321 μM), Hill coefficient (1.01) and the τ_{max} and τ_{min} determined during calibration as reported in [62]:

$$[Ca^{2+}] \approx K_D\left(\frac{\tau_{\max} - \tau_{\exp}}{\tau_{\exp} - \tau_{\min}}\right)^{1/h}. \tag{13}$$

G. Measurement of total Ca^{2+} load

To measure total Ca^{2+} load in the ER lumen, COS-7 cells (WT, RTN3 OE monitored by labelling with JF646, ATL2/3 KO lines) were transfected to express GCaMP3-ER probe, an ER membrane-tethered Ca^{2+} sensor facing cytosolic side [74], and 48h post-transfection, cells were taken to microscopy. Cells were treated with thapsigargin (1 μM) to inhibit the SERCA pump and deplete ER Ca^{2+}. We used a confocal microscope (STELLARIS8, Leica, Wetzlar, Germany) with a controlled environment (37°C, 5% CO_2) with excitation/emission of $480/485-550$ nm with 0.1 frames per second for 10 minutes post treatment. Peaks indices and lowest contour lines were automatically detected and used to quantify the Area Under the Peak with the composite trapezoidal rule in Python.

H. Local Ca^{2+} release events generation, imaging, and analysis

1. Image acquisition

COS-7 cells (WT, RTN3 OE monitored by labelling with JF646, ATL2/3 KO lines) were transfected to ex-

press GCaMP3-ER probe, and 48h post-transfection, cells were taken to microscopy. Local release was achieved by treating cells with caged-IP3 (3 μM, 2.5 hours) followed by low amounts of Bapta-AM (30nM, 5min), a cell permeant chelator. The cytoplasmic chelation by Bapta-AM helped prevent the formation of intracellular Ca^{2+} waves upon delivery of caged-IP3 over the whole cell, allowing measurement of local Ca^{2+} events at sites of initiation. We used a confocal microscope (STELLARIS8, Leica, Wetzlar, Germany) with a controlled environment (37°C, 5% CO_2) and the following parameters: excitation/emission of $480/485 - 550$ nm, frame size of 512×256 pixels, scan speed of 800 Hz bidirectional, 3 frames per second. Image acquisition series consisted of pre-photo-uncaging images (50 frames), photo-uncaging of caged-iP3 achieved by short illumination (405 nm, 50% laser power) across the whole cell using the Fly mode in the FRAP wizard (time interval 331ms), and post-photo-uncaging images (150 frames). The 405nm laser pulse duration was determined to trigger local releases only, while avoiding the induction of global Ca^{2+} waves across the cytoplasm. we assessed the threshold for wave trigger and then induced local Ca^{2+} release events at a regime just under those parameter by reducing the duration of laser pulse.

Local releases were then analyzed semi-automatically as described in the following section.

2. *Image analysis*

The magnitude of local Ca^{2+} transients was determined via image analysis using a custom code written in Matlab [75]. The images of Ca^{2+} sensor GCaMP3-ER during post-photo-uncaging image series were used. Cell shape was manually segmented and the resulting ROI consisted of the area within cell boundary. This ROI was sub-divided by tiling the cell area into a set of rectangular regions of size 25×25 pixels. Signal traces from each rectangular sub-region were plotted and used to search for peaks in the resulting signal traces. Filtering for peaks was achieved by detrending the signal with polynomial fit (order 3) followed by SVG smoothing (order 5, window size 15).

Signal peaks were identified by thresholding using a universal threshold based on the median absolute deviation of the detrended signal [76]. In addition, the detrended signal curvature was computed at each peak, and only those peaks with negative curvature beyond a threshold value (set to $0.1\times$ the universal threshold) were retained for further analysis. ROIs with similar peak positions in time (according to a set cutoff for time separation) and adjacent in space were combined together to prevent similar Ca^{2+} signals to be measured through several ROIs. The peak Ca^{2+} signal within the merged cluster of regions was identified and used to create a new rectangular ROI centered on that peak (35×35 pixels). Signal traces were extracted from these new ROIs and peak detection again applied, using the same threshold values. A total of 59, 28 and 47 peaks were analyzed for WT, RTN3 OE and ATL dKO respectively. The integral of the area under the peak was found by approximating each peak as a Gaussian shape of a fitted width as given by Matlab's 'findpeaks' function. The peak integrals were used as a measure of the magnitude of Ca^{2+} release in the ROI.

The code for analysing local Ca^{2+} releases is available on `https://github.com/lenafabr/photoActivationAnalysis/roisignalGUI.git`

VI. SUPPLEMENTARY MATERIAL

A. Cytoplasmic buffer proteins in local release model

The levels of free Ca^{2+} in the cytoplasm surrounding the release site can be modulated by binding of Ca^{2+} to buffer proteins. Because estimates for the density and binding strength of cytoplasmic Ca^{2+} buffers vary widely, we consider a range of values here, with the goal of demonstrating that the presence of buffers cannot substantially increase the local concentration of free Ca^{2+}.

We incorporate cytoplasmic buffers into our model for purely local release numerically, using a finite-volume approach in radial coordinates and assuming equilibrated binding. The unbound Ca^{2+} density $\psi_u(\rho, t)$ and bound Ca^{2+} density $\psi_b(\rho, t)$ (as a function of radial distance ρ from the release site) obey the following dynamic equation:

$$\frac{d\psi}{dt} = D_{\text{cyto}}\nabla^2\psi_u + D_{\text{b,cyto}}\nabla^2\psi_b + J(t)\frac{\delta(\rho)}{4\pi\rho^2}, \quad \text{(S1)}$$

where $D_{\text{cyto}} = 200\mu\text{m}^2/\text{s}$ and $D_{b,\text{cyto}} = 2\mu\text{m}^2/\text{s}$ are diffusivities of free Ca^{2+} and buffer proteins, respectively, $J(t)$ is the release current, and δ is the Dirac delta function. The equilibrium condition is expressed as

$$K_{D,\text{cyto}} = \frac{\psi_u(S_{\text{cyto}} - \psi_b)}{\psi_b}, \quad \text{(S2)}$$

where $K_{D,\text{cyto}}$ is the cytoplasmic buffer binding strength and S_{cyto} is the (constant) density of cytoplasmic buffer binding sites.

To evolve forward Eq. S1, we break up the space surrounding the origin into mesh cells representing spherical shells, of thickness $\Delta\rho$, and volume $V_i = 4\pi\rho_i^2\Delta\rho$, for $i = 1, 2, \ldots$. The innermost mesh cell has volume $V_0 = \frac{4}{3}\pi(\Delta\rho)^3$. The current of free Ca^{2+} through the inner and outer boundary of mesh cell i is then

$$\begin{aligned} \mathcal{I}^u_{i-1/2} &= D_{\text{cyto}}4\pi\left(\rho_i - \frac{\Delta\rho}{2}\right)^2 \frac{(\psi_{u,i} - \psi_{u,i-1})}{\Delta\rho} \\ \mathcal{I}^u_{i+1/2} &= D_{\text{cyto}}4\pi\left(\rho_i + \frac{\Delta\rho}{2}\right)^2 \frac{(\psi_{u,i+1} - \psi_{u,i})}{\Delta\rho}, \end{aligned} \quad \text{(S3)}$$

with analogous expressions for the diffusive current of bound Ca^{2+}. At each time-step, we compute the change in total Ca^{2+} in each mesh cell due to diffusive current, analogous to Eq. 10 but with the area of each boundary already incorporated into the current. Additionally, the innermost cell ($i = 0$) concentration is updated due to the Ca^{2+} release according to $J(t)\Delta t/V_0$. The total Ca^{2+} field is evolved forward in time-steps of $\Delta t = 10^{-5}$s, and the unbound and bound Ca^{2+} fields are concurrently updated via Eq. S2.

The cytoplasmic free Ca^{2+} concentration is averaged over a sphere of radius $R_{\text{loc}} = 1\mu$m and plotted versus time in Fig. S1b. Increasing the buffer concentration slows the spread of Ca^{2+} from the release site, but also decreases the fraction of cytoplasmic Ca^{2+} that is free from buffer binding. Parameter sweeps for different values of membrane permeability P and cytoplasmic buffer binding strength $K_{d,\text{cyto}}$ indicate that the free Ca^{2+} concentration around the release site at 0.1s never rises above 30nM, regardless of how many cytoplasmic buffer sites are present (Fig. S1c,d).

B. Luminal buffer carrying capacity

Throughout the calculations in the main text, we make a conservative estimate of the luminal Ca^{2+} carrying capacity. Namely, we assume that buffer protein concentration is 0.1mM and that each protein contains 25 Ca^{2+} binding sites ($S = 2.5$mM). Given the presence of multiple luminal Ca^{2+} buffers, the actual capacity is likely to be higher. As a consequence, purely local release from an isolated region of size $R = 0.25\mu$m will result in higher cytoplasmic Ca^{2+} concentrations with higher values of S (Fig. S2). However, we note that even an order-of-magnitude increase in buffer sites (to $S = 25$mM), will result in cytoplasmic Ca^{2+} concentrations below 200nM at 0.1sec after the start of release. These concentrations drop still further at subsequent times. We therefore maintain that purely local release is insufficient to maintain the observed magnitudes of Ca^{2+} puffs (which can range up to 1μM in osteoclasts [27]), even in the case where the luminal Ca^{2+} capacity is substantially higher.

For the spatial model incorporating transport through the ER network, the results presented in this work become even more pronounced if there is a higher concentration of luminal buffer sites. Specifically, the enhancement in Ca^{2+} release at the optimal binding strength K_d is greater with increasing buffer capacity (Fig. S3a). The value of that optimal strength remains at $K_d^{\text{opt}} \approx 0.2$mM over a broad range of buffer concentrations. Furthermore, the effect of luminal buffer protein mobility, both with and without active flow within the ER tubules, is augmented when there are more buffer proteins present (Fig. S3b, compare to Fig. 2h).

C. Optimal buffer strength for different permeabilities

In the model incorporating Ca^{2+} and buffer transport through a network, the optimum buffer binding strength is robust over a broad range of time-scales (Fig. 4e). However, this optimal binding strength does depend on the permeability P and extent R of the local release region. When the leaking of Ca^{2+} from the release region is much slower than its diffusive delivery from elsewhere in the lumen, the local free Ca^{2+} concentration is maintained close to its original value of $U_0 = 0.5$mM, and the optimal binding strength $K_D^{\text{opt}} \to 0.5$mM concomitantly (Fig. S4). By contrast, when local release is much

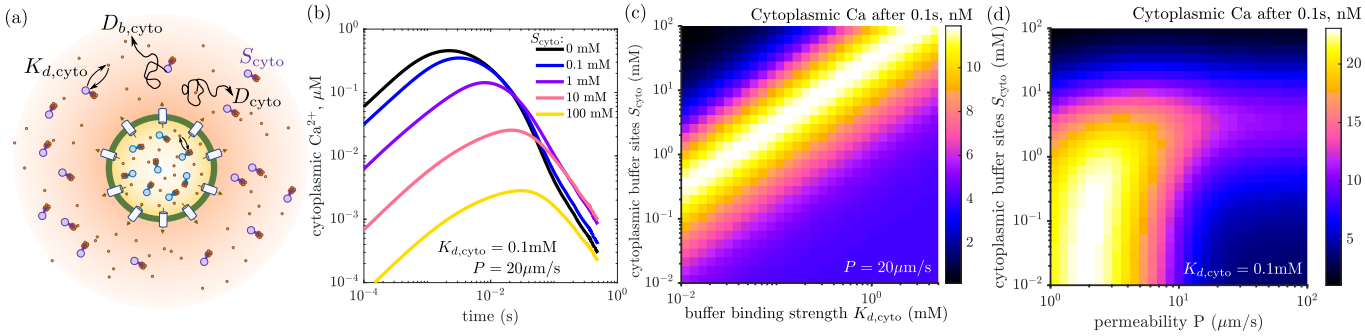

FIG. S1. Cytoplasmic Ca^{2+} levels with inclusion of cytoplasmic buffer binding, for model with release of local Ca^{2+} pool only (no luminal transport). (a) Model schematic, indicating equilibrated binding to diffusive buffer sites in the cytoplasm. (b) Cytoplasmic Ca^{2+} concentration (in μM) near release site over time, for several different densities of cytoplasmic binding sites S_{cyto}. (c) Averaged cytoplasmic Ca^{2+} level (in nM) near release site, as a function of cytoplasmic buffer site density S_{cyto} and cytoplasmic buffer strength $K_{d,\mathrm{cyto}}$. (d) Averaged cytoplasmic Ca^{2+} near release site as a function of buffer site density and permeability of local release region P. Ca^{2+} concentrations are shown at time $t = 0.1$ sec, as an average over a sphere of radius $R_{\mathrm{loc}} = 1\mu$m, centered on the release site. Total length of releasing tubules is set to $L = 0.75\mu$m, cytoplasmic Ca^{2+} diffusivity is $D_{\mathrm{cyto}} = 200\mu\mathrm{m}^2/\mathrm{s}$, and cytoplasmic buffer diffusivity is $D_{b,\mathrm{cyto}} = 2\mu\mathrm{m}^2/\mathrm{s}$.

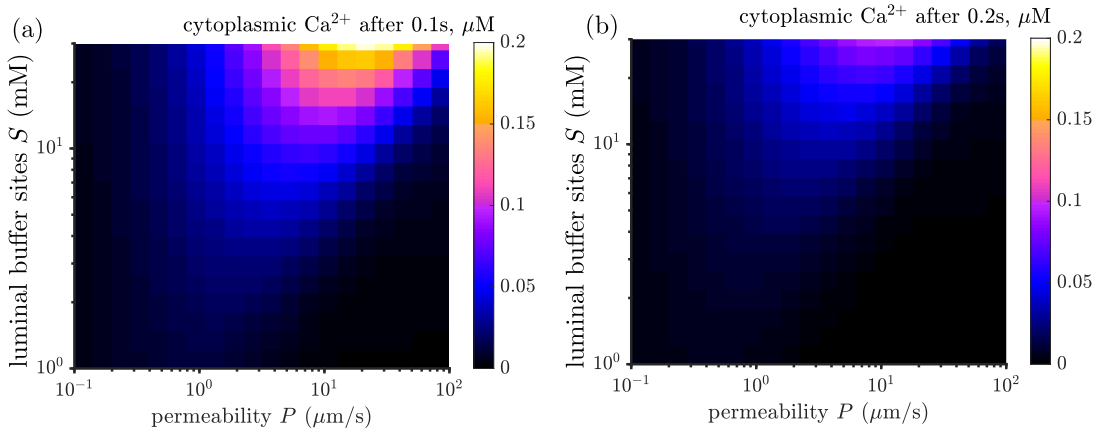

FIG. S2. Cytoplasmic Ca^{2+} levels from purely local release vary with luminal Ca^{2+} carrying capacity. (a) Cytoplasmic Ca^{2+} concentration averaged over a region of radius $R_{\mathrm{loc}} = 1\mu$m, at time $t = 0.1$sec, plotted as a function of membrane permeability P and concentration of luminal binding sites S. (b) Corresponding plot for local cytoplasmic Ca^{2+} at $t = 0.2$sec.

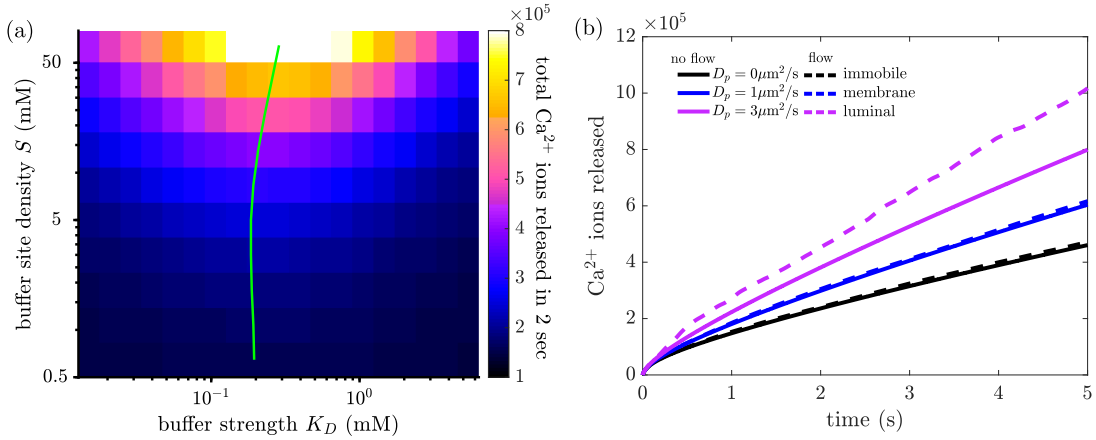

FIG. S3. Ca^{2+} release from honeycomb network with increased luminal buffer site concentration. (a) Cumulative Ca^{2+} release in 2sec, as a function of buffer binding strength K_D and concentration of luminal buffer sites S. Green line shows optimal binding strength for each value of S. (b) Cumulative Ca^{2+} release over time for buffer proteins with different diffusivities, with (dashed lines) and without (solid lines) ER luminal flows. Results shown assume a buffer site density of $S = 10$mM. Compare to Fig. 2h, which uses $S = 2.5$mM.

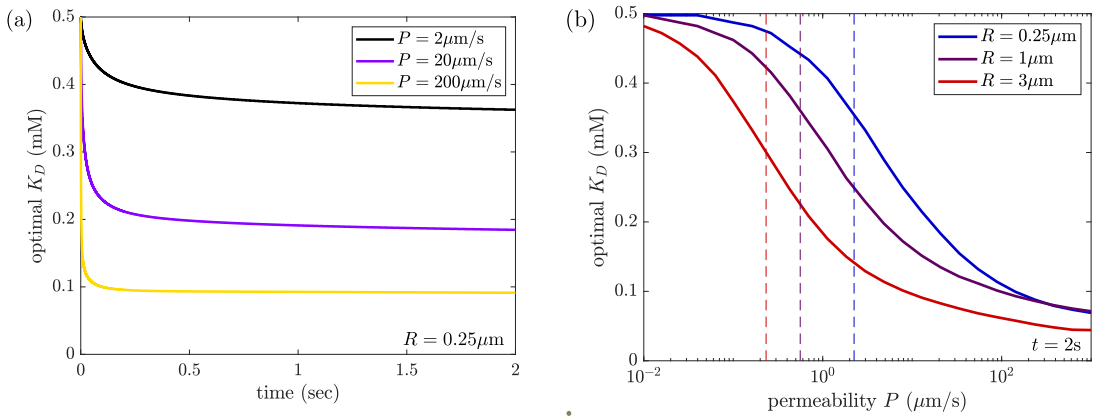

FIG. S4. Effect of permeability and release region size on optimal buffer strength. (a) Value of binding strength K_D that maximizes the cumulative amount of Ca^{2+} released by a certain time, plotted as a function of time. Each curve corresponds to a different permeability of the release region. The optimal K_D is robust over a broad range of times. (b) Optimal binding strength K_D that maximizes cumulative Ca^{2+} release in 2s, plotted versus the permeability P. Each curve corresponds to a different radius of the release region (R). Dashed lines show estimated critical permeability P^* beyond which Ca^{2+} transport becomes rate-limiting an local Ca^{2+} levels are depleted. Below P^*, the optimal binding strength matches the initial free Ca^{2+} ($U_0 = 0.5$mM). Above P^*, the optimal K_D drops to lower concentrations.

faster than diffusive delivery, the local Ca^{2+} concentration drops and K_D^{opt} becomes smaller, in order to maximize the total amount of Ca^{2+} ions stored in the lumen.

The fully connected honeycomb network considered here can be approximately treated as an effective two-dimensional continuum, with the initial free Ca^{2+} concentration per unit area given by $\widehat{U}_{2D} = U\pi r^2\rho$, where U is the concentration of free Ca^{2+} in the lumen and ρ is the density of ER tubule length per unit area. For a honeycomb network with edges of length ℓ, this density is $\rho = 2/(\sqrt{3}\ell)$. To estimate the rate of arrival to the release region, we use the long-time limit for two-dimensional diffusive current to a region of size R_{eff}, assuming an effective diffusivity $D/2$ [52]:

$$k_{2\text{D}} \approx \frac{2\pi D\widehat{U}_{2D}}{\log(2Dt/R_{\text{eff}}^2) - 2\gamma}, \tag{S4}$$

where $\gamma \approx 0.58$ is the EulerMascheroni constant. This expression takes into account the factor of 2 reduction in effective 2D diffusivity due to confinement in a lattice of tubules [56]. The effective capture radius is set to $R_{\text{eff}} = \max(R, \ell)$, corresponding to the distance where the tubules leading to a small release region join the rest of the lattice, or else to the size of an entire larger release region. The logarithmic term implies that the diffusive delivery (and hence the local Ca^{2+} concentration) is not very sensitive to time, and helps explain the lack of time-sensitivity for K_D^{opt}.

The local release current from a permeable region with total tube length L is given by $k_{\text{release}} = P(2\pi r)L$. As shown in Fig. S4b, the optimum binding strength K_D^{opt} transitions from U_0 down to 0mM when the permeability passes a critical value P^*. This value corresponds to the transition when release rates exceed diffusive delivery rates: $k_{\text{release}} > k_{2\text{D}}$, which corresponds to

$$P \gg P^* = \frac{\pi D r \rho}{L(\log(2Dt/R_{\text{eff}}^2) - 2\gamma)}. \tag{S5}$$

Here L is the length of tubule in the releasing region ($L = 3R$ for $R < \ell$ and $L = \pi R^2\rho$ for $R >> \ell$). Notably, for large release regions, the critical permeability is independent of tubule density as the lattice behaves simply as an effective 2D continuum.

D. Alternate assumptions for release from perturbed network structures

The highly simplified network structures employed for the Ca^{2+} release simulations serve to highlight key qualitative features of the ER morphological permutations, rather than providing a detailed replica of the perturbed morphology. In addition, our attribution of reduced Ca^{2+} release to changes in network structure relies on the assumption that the free Ca^{2+} concentration and the total buffer protein content are unchanged upon morphological perturbation. In Fig. 5c, we show that the free Ca^{2+} concentration changes only slightly (from approximately 0.5mM in WT cells to approximately 0.6mM in RTN3 OE and ATL dKO cells). Supplemental figure S5a demonstrates that this small increase in free Ca^{2+} does not alter the prediction of reduced Ca^{2+} release in perturbed structures.

In Fig. 5d-e, the total Ca^{2+} load inside the ER is shown to be not significantly different in the perturbed cells. As discussed in the main text, our model bubbled network structure, with bubbles of radius 0.3μm implies that the total volume of the ER should increase by roughly 3-fold, and the total Ca^{2+} load (under the assumption that the

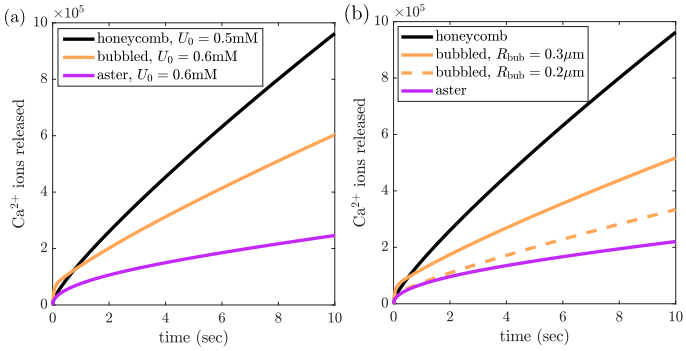

FIG. S5. Release from different network structures, as in Fig. 4a. (a) Initial free Ca^{2+} concentration in the perturbed network structures (bubbled and aster) is set to 0.6mM, as measured via FLIM (Fig. 5c). (b) Bubble radius in structure representing RTN3 OE cells is varied from 0.3μm (solid line) to 0.2μm (dashed line). Total protein content and free Ca^{2+} concentration is assumed to stay constant as compared to WT cells. All other parameters are as in Fig. 4b.

total number of buffer proteins stays constant) should increase by approximately 40%. This modest predicted increase is not seen in the experimental data. We note that our approximation of bubble size and shape in the RTN3 OE cells is quite rough, as the bubbles are imaged in two dimensions and with standard optical resolution. For example, reducing bubble radius to 0.2μm would imply a volume increase above the WT network of only 60% and an increase in total calcium load of only 12%. In this case, the predicted Ca^{2+} release from a localized region would be even lower (Fig. S5). Overall, our measurements indicate that neither changes in luminal free Ca^{2+} nor changes in the total amount of Ca^{2+} stored in the ER account for the measured reduction in local Ca^{2+} release events. Simulated results in our simplified network models imply that the change in ER luminal connectivity could lead to the observed reduction in Ca^{2+} release.

VII. ACKNOWLEDGMENTS

We thank Laura Westrate for helpful discussions. EFK is funded by NSF award #2034482, a Cottrell Scholar Award from the Research Corporation for Science Advancement, and a UCSD Chancellor Funded Research Grant. EA is supported by the UK Dementia Research Institute [award number UK DRI-2004] which receives its funding from UK DRI Ltd, funded by the UK Medical Research Council, Alzheimers Society and Alzheimers Research UK.

[1] G. K. Voeltz, M. M. Rolls, and T. A. Rapoport, EMBO reports **3**, 944 (2002).
[2] Y. Shibata, G. K. Voeltz, and T. A. Rapoport, Cell **126**, 435 (2006).
[3] C. Blackstone, Annual Review of Neuroscience **35**, 25 (2012).
[4] M. G. Sharoar, Q. Shi, Y. Ge, W. He, X. Hu, G. Perry, X. Zhu, and R. Yan, Molecular Psychiatry **21**, 1263 (2016).
[5] Z. Ozturk, C. J. OKane, and J. J. Prez-Moreno, Frontiers in Neuroscience **14** (2020), 10.3389/fnins.2020.00048.
[6] L. M. Westrate, J. E. Lee, W. A. Prinz, and G. K. Voeltz, Annual Review of Biochemistry **84**, 791 (2015).
[7] H. Wu, P. Carvalho, and G. K. Voeltz, Science **361**, eaan5835 (2018).
[8] T. Konno, P. Parutto, D. M. Bailey, V. Davì, C. Crapart, M. A. Awadelkareem, C. Hockings, A. Brown, K. M. Xiang, A. Agrawal, *et al.*, bioRxiv (2021).
[9] I. Parker and I. Ivorra, Science (New York, N.Y.) **250**, 977 (1990).
[10] Y. Yao and I. Parker, The Journal of Physiology **476**, 17 (1994).
[11] M. Bootman, E. Niggli, M. Berridge, and P. Lipp, The Journal of Physiology **499**, 307 (1997).
[12] I. F. Smith, S. M. Wiltgen, and I. Parker, Cell calcium **45**, 65 (2009).
[13] J. T. Low, A. Shukla, and P. Thorn, The International Journal of Biochemistry & Cell Biology **42**, 1586 (2010).
[14] H. Cheng, W. J. Lederer, and M. B. Cannell, Science **262**, 740 (1993).
[15] E. Niggli, Annual review of physiology **61**, 311 (1999).
[16] S. Koizumi, M. D. Bootman, L. K. Bobanovi, M. J. Schell, M. J. Berridge, and P. Lipp, Neuron **22**, 125 (1999).
[17] S. Manita and W. N. Ross, Journal of Neuroscience **29**, 7833 (2009).
[18] A. Volterra, N. Liaudet, and I. Savtchouk, Nature Reviews Neuroscience **15**, 327 (2014).
[19] N. Bazargani and D. Attwell, Nature Neuroscience **19**, 182 (2016).
[20] A. Semyanov, C. Henneberger, and A. Agarwal, Nature Reviews Neuroscience **21**, 551 (2020).
[21] M. J. Berridge, Journal of Experimental Biology **200**, 315 (1997).
[22] K. A. Woll and F. V. Petegem, Physiological Reviews **102**, 209 (2022).
[23] I. Parker, J. Choi, and Y. Yao, Cell Calcium **20**, 105 (1996).
[24] Y. Yao, J. Choi, and I. Parker, The Journal of Physiology **482**, 533 (1995).
[25] J. Keizer, G. D. Smith, S. Ponce-Dawson, and J. E. Pearson, Biophysical journal **75**, 595 (1998).
[26] M. Endo, Physiological Reviews **89**, 1153 (2009).
[27] W. Radding, S. E. Jordan, R. B. Hester, and H. C. Blair, Experimental Cell Research **253**, 689 (1999).
[28] L. Bruno, G. Solovey, A. C. Ventura, S. Dargan, and S. P. Dawson, Cell calcium **47**, 273 (2010).
[29] X.-P. Sun, N. Callamaras, J. S. Marchant, and I. Parker, J Physiol **509**, 67 (1998).
[30] Z. C. Scott, A. I. Brown, S. S. Mogre, L. M. Westrate, and E. F. Koslover, Eur Phys J E **44**, 1 (2021).
[31] D. E. Clapham, Cell **131**, 1047 (2007).
[32] S. A. Jimenez, P. Dehm, B. R. Olsen, D. J. Prock-op, J. B. Chern, and J. Uitto, Science **190**, 1204 (1975).
[33] B. Schwaller, Cold Spring Harbor Perspectives in Biology **2**, a004051 (2010).
[34] F. Wuytack, L. Raeymaekers, and L. Missiaen, Cell Calcium **32**, 279 (2002).
[35] S. Baksh and M. Michalak, Journal of Biological Chemistry **266**, 21458 (1991).
[36] Z. Yang and E. F. Koslover, Physical Biology (2023).
[37] Y. Okubo and M. Iino, The Journal of physiology **598**, 1671 (2020).
[38] M. Brini, D. Bano, S. Manni, R. Rizzuto, and E. Carafoli, The EMBO Journal **19**, 4926 (2000).
[39] W.-A. Wang, L. B. Agellon, and M. Michalak, Cold Spring Harbor Perspectives in Biology **11**, a038265 (2019).
[40] M. Michalak, J. Groenendyk, E. Szabo, L. I. Gold, and M. Opas, Biochemical Journal **417**, 651 (2009).
[41] K.-H. Krause and M. Michalak, Cell **88**, 439 (1997).
[42] A. J. Laude and A. W. Simpson, The FEBS journal **276**, 1800 (2009).
[43] M. T. Alonso, M. J. Barrero, P. Michelena, E. Carnicero, I. Cuchillo, A. G. García, J. García-Sancho, M. Montero, and J. Alvarez, The Journal of cell biology **144**, 241 (1999).
[44] J. Meldolesi and T. Pozzan, Trends in biochemical sciences **23**, 10 (1998).
[45] J. A. Gilabert, "Cytoplasmic calcium buffering," in *Calcium Signaling*, edited by M. S. Islam (Springer Netherlands, Dordrecht, 2012) pp. 483–498.
[46] E. A. Matthews and D. Dietrich, Frontiers in cellular neuroscience , 48 (2015).
[47] E. Niggli and N. Shirokova, Cell calcium **42**, 379 (2007).
[48] D. Thomas, P. Lipp, M. J. Berridge, and M. D. Bootman, Journal of Biological Chemistry **273**, 27130 (1998).
[49] I. Parker and Y. Yao, The Journal of Physiology **491**, 663 (1996).
[50] H. T. Perkins, V. J. Allan, and T. A. Waigh, Scientific Reports **11**, 16230 (2021).
[51] L. K. Schroeder, A. E. Barentine, H. Merta, S. Schweighofer, Y. Zhang, D. Baddeley, J. Bewersdorf, and S. Bahmanyar, Journal of Cell Biology **218**, 83 (2019).
[52] S. Redner, *A guide to first-passage processes* (Cambridge University Press, 2001).
[53] P. D. Nash, M. Opas, and M. Michalak, Molecular and cellular biochemistry **135**, 71 (1994).
[54] D. Holcman, P. Parutto, J. E. Chambers, M. Fantham, L. J. Young, S. J. Marciniak, C. F. Kaminski, D. Ron, and E. Avezov, Nat Cell Biol **20**, 1118 (2018).
[55] M. Dora and D. Holcman, Proceedings of the Royal Society B **287**, 20200493 (2020).
[56] Y. Sun, Z. Yu, C. J. Obara, K. Mittal, J. Lippincott-Schwartz, and E. F. Koslover, Physical Review Research **4**, 023182 (2022).
[57] E. Dudek and M. Michalak, Encyclopedia of Metalloproteins; Kretsinger, RH, Uversky, VN, Permyakov, EA, Eds , 555 (2013).
[58] P. Grumati, G. Morozzi, S. Hlper, M. Mari, M. L. I. Harwardt, R. Yan, S. Mller, F. Reggiori, M. Heilemann,

and I. Dikic, eLife **6** (2017), 10.7554/eLife.25555.
[59] J. Espadas, D. Pendin, R. Bocanegra, A. Escalada, G. Misticoni, T. Trevisan, A. Velasco del Olmo, A. Montagna, S. Bova, B. Ibarra, *et al.*, Nature communications **10**, 5327 (2019).
[60] S. Wang, H. Tukachinsky, F. B. Romano, and T. A. Rapoport, Elife **5**, e18605 (2016).
[61] M. S. Tikhomirova, A. Kadosh, A. J. Saukko-Paavola, T. Shemesh, and R. W. Klemm, Proceedings of the National Academy of Sciences **119**, e2104309119 (2022).
[62] E. Greotti, A. Wong, T. Pozzan, D. Pendin, and P. Pizzo, Sensors (Switzerland) **16** (2016), 10.3390/s16091419.
[63] E. Sammels, J. B. Parys, L. Missiaen, H. D. Smedt, and G. Bultynck, Cell Calcium **47**, 297 (2010).
[64] I. F. Smith and I. Parker, Proceedings of the National Academy of Sciences **106**, 6404 (2009).
[65] M. Chen, M. J. Van Hook, and W. B. Thoreson, Journal of Neuroscience **35**, 11364 (2015).
[66] T. GrandPré, F. Nakamura, T. Vartanian, and S. M. Strittmatter, Nature **403**, 439 (2000).
[67] V. Pernet, S. Joly, D. Dalkara, O. Schwarz, F. Christ, D. Schaffer, J. Flannery, and M. Schwab, Cell Death & Differentiation **19**, 1096 (2012).
[68] K. Kanemaru, H. Sekiya, M. Xu, K. Satoh, N. Kitajima, K. Yoshida, Y. Okubo, T. Sasaki, S. Moritoh, H. Hasuwa, *et al.*, Cell reports **8**, 311 (2014).
[69] N. L. Allbritton, T. Meyer, and L. Stryer, Science **258**, 1812 (1992).
[70] J.-Y. Tinevez, N. Perry, J. Schindelin, G. M. Hoopes, G. D. Reynolds, E. Laplantine, S. Y. Bednarek, S. L. Shorte, and K. W. Eliceiri, Methods **115**, 80 (2017).
[71] W. H. Hundsdorfer, J. G. Verwer, and W. Hundsdorfer, *Numerical solution of time-dependent advection-diffusion-reaction equations*, Vol. 33 (Springer, 2003).
[72] O. Bénichou, C. Chevalier, J. Klafter, B. Meyer, and R. Voituriez, Nature chemistry **2**, 472 (2010).
[73] D. S. Grebenkov and D. Krapf, The Journal of Chemical Physics **149**, 064117 (2018).
[74] S. Mehta, N. N. Aye-Han, A. Ganesan, L. Oldach, K. Gorshkov, and J. Zhang, eLife **3**, 1 (2014).
[75] T. M. Inc., "Matlab version: 9.13.0 (r2022b)," (2022).
[76] K. Chen, B. Wang, J. Guan, and S. Granick, Acs Nano **7**, 8634 (2013).